The Astrophysical Journal, 539:865–887, 2000 August 20

A NEW ALGORITHM FOR SUPERNOVA NEUTRINO TRANSPORT AND SOME APPLICATIONS

Adam Burrows,[1] Timothy Young,[1] Philip Pinto,[1,2] Ron Eastman,[2,3] and Todd A. Thompson[4]

Received 1999 May 11; accepted 2000 March 29

ABSTRACT

We have developed an implicit, multigroup, time-dependent, spherical neutrino transport code based on the Feautrier variables, the tangent-ray method, and accelerated Λ iteration. The code achieves high angular resolution, is good to $O(v/c)$, is equivalent to a Boltzmann solver (without gravitational redshifts), and solves the transport equation at all optical depths with precision. In this paper, we present our formulation of the relevant numerics and microphysics and explore protoneutron star atmospheres for snapshot postbounce models. Our major focus is on spectra, neutrino-matter heating rates, Eddington factors, angular distributions, and phase-space occupancies. In addition, we investigate the influence on neutrino spectra and heating of final-state electron blocking, stimulated absorption, velocity terms in the transport equation, neutrino-nucleon scattering asymmetry, and weak magnetism and recoil effects. Furthermore, we compare the emergent spectra and heating rates obtained using full transport with those obtained using representative flux-limited transport formulations to gauge their accuracy and viability. Finally, we derive useful formulae for the neutrino source strength due to nucleon-nucleon bremsstrahlung and determine bremsstrahlung's influence on the emergent ν_μ and ν_τ neutrino spectra. These studies are in preparation for new calculations of spherically symmetric core-collapse supernovae, proto–neutron star winds, and neutrino signals.

Subject headings: elementary particles — methods: numerical — radiative transfer — stars: interiors — stars: neutron — supernovae: general

1. INTRODUCTION

With core-collapse supernova explosions, nature has contrived an elegant means to create compact objects while at the same time seeding the galaxy with the elements of existence. Neutrinos play a key role in the phenomena of collapse and explosion, for not only are they produced in abundance at the high temperatures and densities achieved in collapse, but they are weakly enough coupled to matter that they transport heat and leptons on a dynamically interesting timescale. It is now thought that neutrino heating of the protoneutron star mantle drives the supernova explosion (Colgate & White 1966; Bethe & Wilson 1985), but only after a postbounce delay of hundreds of milliseconds to 1 s. During this delay, the quasi-static accreting core, the proto–neutron star bounded by the stalled shock wave, radiates neutrinos of all species and the net energy deposition in the semitransparent "gain region" behind the shock plays a pivotal role in "igniting" the explosion. However, the precise deposition rate depends upon the details of neutrino transfer at low "optical" depths, putting great demands upon the theoretical tools employed to calculate the properties of the neutrino radiation fields. The character of that radiation depends upon neutrino-matter opacities, neutrino production source terms, and neutrino transport. Over the years, neutrino transport theory and the associated microphysics have reached a sophisticated level of refinement (Tubbs & Schramm 1975; Lichtenstadt et al. 1978; Bowers & Wilson 1982; Mayle, Wilson, & Schramm 1987; Bludman & Schinder 1988; Bruenn 1985; Janka 1991; Mezzacappa & Bruenn 1993a, 1993b; Messer et al. 1998; Yamada, Janka, & Suzuki 1999). However, despite these efforts, recent progress in modeling supernovae, and new insights gained into the character of multidimensional neutrino-driven explosions (Herant et al. 1994; Burrows, Hayes, & Fryxell 1995; Janka & Müller 1996; Mezzacappa et al. 1998), the supernova explosion problem is not solved in detail. We know little about the dependence of the ^{56}Ni yields on progenitor mass and composition, the iron-peak nucleosynthesis, the explosion energies, the nascent pulsar kicks, and the asymmetries and mixing in the explosion debris. Furthermore, we still do not know the duration of the postbounce delay, nor the ensemble of possible neutrino signatures.

In the past, a variety of approximations to the full neutrino transport equations have been employed in complex numerical codes meant to simulate stellar collapse and supernova explosions. These compromises have been deemed necessary because of the severe CPU constraints of such simulations, particularly when those simulations have been multidimensional (Herant et al. 1994; Burrows et al. 1995; Janka & Müller 1996). A variety of gray approaches, flux limiters, equilibrium assumptions, and approximations to both neutrino source and redistribution terms have been employed, sometimes to good effect. However, given the marginality of the explosions thus far obtained, the fact that there is as yet no unanimity among theorists concerning important issues of principle (cf. Mezzacappa et al. 1998), and the manifest importance of neutrinos in collapse phenomenology, a fresh look at neutrino transport and the relevant neutrino physics is in order. It is in that spirit that we have constructed an implicit, time-dependent, multigroup, multiangle, multispecies neutrino transfer code to simulate the neutrino radiation fields in stellar collapse and explosion. This code embodies a different computational method from that used in the pioneering papers by Bruenn (1985) and Mezzacappa (Mezzacappa & Bruenn 1993a,

[1] Department of Astronomy and Steward Observatory, University of Arizona, Tucson, AZ 85721; aburrows@as.arizona.edu, tyoung@as.arizona.edu, ppinto@as.arizona.edu.
[2] Lawrence Livermore National Laboratory, Livermore, CA 94551.
[3] Department of Astronomy and Astrophysics, University of California, Santa Cruz, CA 95064; reastman@llnl.gov.
[4] Department of Physics, University of Arizona, Tucson, AZ 85721; thomp@physics.arizona.edu.

1993b), but in its use of Feautrier variables and the tangent-ray method it is quite in keeping with traditional photon transport and stellar atmospheres simulations (Mihalas 1980; Mihalas & Mihalas 1984). In this paper, we describe the basic algorithm, discuss and derive the relevant neutrino microphysics, and present high-resolution (in energy, angle, and radius) results for representative postbounce proto–neutron star configurations. Hence, for this first paper in our series on neutrino transport and microphysics we focus on precision neutrino "atmospheres." We present the energy spectra, Eddington factors, angular distributions, phase space densities, and neutrino-matter energy couplings. We also derive or discuss the relevant neutrino physics, some of it new. We calculate the background neutrino radiation fields for two snapshot models, one of which is from the work of Burrows et al. (1995) representing the wind phase that follows explosion (model W), and one of which (our model BM) was kindly provided to us by T. Mezzacappa and is from a multigroup, flux-limited diffusion simulation by Bruenn (Messer et al. 1998), 106 ms after the bounce of the core of a Weaver & Woosley (1995) 15 $M_\odot$ star. These are meant to exemplify various proto–neutron star structures and phases for the purposes of a detailed scrutiny of the neutrino sector. Consistent dynamical calculations will follow later in the series.

Neutrinos are the major signatures of the inner turmoil of the dense core of the massive star, and they carry away the binding energy of the young neutron star, a full 10% of its mass energy. The detection of collapse neutrinos, their "light curve" and spectra, will allow us to follow in real time the phenomena of stellar death and birth. The supernova, SN 1987A, provided a glimpse of what might be possible, but it yielded only 19 events; we can expect the current generation of underground neutrino telescopes to collect thousands of events from a Galactic supernova.

In § 2, we present the equations and physics of neutrino transport. In § 3 we describe our implementation of the Feautrier and tangent-ray schemes, and we follow this in § 4 with a discussion of accelerated Λ iteration and our approach to the implicit coupling of matter with neutrino radiation. Section 5 contains a physical derivation of stimulated absorption, and § 6 summarizes the cross sections and source terms we employ for this study. We provide in § 7 a derivation of the single and pair neutrino rates and spectra due to nucleon-nucleon bremsstrahlung, a process that can compete with pair annihilation as a source for ν_μ, $\bar{\nu}_\mu$, ν_τ, and $\bar{\nu}_\tau$ neutrinos and that to date has not been incorporated into supernova codes. (The consequences of bremsstrahlung for the emergent ν_μ spectra are presented in § 10.) In § 8, we present for generic protoneutron star configurations our basic results vis à vis emergent energy spectra, luminosities, and energy deposition rates (including that due to $\nu\bar{\nu}$ annihilation). We also explore the dependence of the emergent spectra and neutrino heating rates on blocking factors, weak magnetism and recoil, aberration and Doppler terms, and stimulated absorption. These terms/effects are frequently dropped in simpler schemes. In § 9, we highlight the angular dependence of the radiation fields and the conceptual limitations of flux limiters that ignore the angular dimension. Moreover, we compare the emergent spectra and heating rates obtained using our full transport code with those obtained using representative flux-limiter closures in order to gauge the errors of such approximate schemes.

This paper contains a description of neutrino transfer, our numerical approach, and the new results that flow from it. It is also meant to summarize various useful formulae that others, as they approach the study of supernova neutrino radiation fields, might employ. In assembling the rates and cross sections, we have borrowed from the investigations of Tubbs & Schramm (1975), Bruenn (1985), Janka (1991), Mezzacappa & Bruenn (1993a, 1993b, 1993c), Schinder & Shapiro (1982a, 1982b), and Bowers & Wilson (1982), but we take full responsibility when we have chosen to deviate from the literature.

2. NEUTRINO TRANSPORT EQUATIONS

We have constructed a radiation/hydrodynamic code that solves the three equations of hydrodynamics with the equations of multigroup radiative transfer and composition. The hydro code is a one-dimensional Lagrangian realization of the explicit piecewise parabolic method (PPM) of Colella & Woodward (1984; also see Fryxell, Müller, & Arnett 1991) that is automatically conservative, second-order accurate in space and time and employs a Riemann solver to handle shocks. Radiation is coupled to the matter between the hydro updates in an implicit, operator-split fashion, employing accelerated Λ iteration (ALI) to facilitate the convergence both of the transport solution and of the temperature and composition changes due to transport. Since in this paper we focus on the transport sector of the code and on precision neutrino atmospheres, we postpone to a later paper a discussion of the full hydrodynamic technique and time-dependent results in the stellar collapse and supernova context. Here we describe the radiation equations solved, the algorithm developed to solve them, and the philosophy behind our methods. In later sections, we explore the nature of the neutrino radiation fields in the postbounce and protoneutron star contexts. In addition, we study the influence of various terms and physics on the emergent neutrino spectra and on the neutrino-matter coupling in the semitransparent region between the neutrinospheres and the stalled shock. Energy deposition in this region is thought to be important in igniting and driving the supernova explosion.

Neutrino transport is not an esoteric subject apart from traditional radiative transfer. The same techniques developed for one particle type can be employed for another. For all particles, the solution to the Boltzmann equation is sought. What distinguishes neutrino transport and transfer are the number of neutrino species (six), the particular microphysics of the neutrino-matter interaction (i.e., cross sections, sources), the Fermi statistics of the neutrinos (manifest only in the collision term), and the fact that there is in principle a conserved lepton number. Neutrino oscillations can alter this, but given the particular neutrino masses and oscillation angles suggested by the recent solar and atmospheric neutrino data (Suzuki 1998; Totsuka et al. 2000), oscillations might not dramatically affect supernova dynamics or the neutrino fields in the core (Fuller et al. 1992). (It should be borne in mind that oscillations in the outer envelope of the progenitor massive star or between the supernova and the Earth may alter the signal detected in underground neutrino telescopes.)

There are a variety of ways of writing the transport equation for the specific intensity (I_ν) of the radiation field (Mihalas 1980; Mihalas & Mihalas 1984). In principle, the

Boltzmann equation and the transport equation are equivalent, though the former is written in terms of the invariant phase space density ($\mathscr{F}_\nu$), related one-to-one to the specific intensity through the identity

$$\frac{I(\mu, \varepsilon)}{\varepsilon^3} = \frac{g}{h^3 c^2} \mathscr{F}_\nu , \tag{1}$$

where $g = 1$ for massless neutrinos, $g = 2$ for photons, ε is the particle's energy, and the other symbols have their standard meanings. Sometimes it is said that the Boltzmann equation is more general than the transport equation because it contains a $\dot{\boldsymbol{p}}$ term that for massless particles corresponds to gravitational redshifts. However, there is no reason to exclude such a term from the transport equation, and we will not engage in such distinctions.

One form of the transport equation for I_ν in the comoving frame in spherically symmetric geometry is

$$\begin{aligned}
\frac{1}{c}\frac{DI_\nu}{Dt} &+ \frac{\mu}{r^2}\frac{\partial}{\partial r}(r^2 I_\nu) + \frac{\partial}{\partial \mu} \\
&\times \left\{(1-\mu^2)\left[\frac{1}{r} + \frac{\mu}{c}\left(\frac{v}{r} - \frac{\partial v}{\partial r}\right)\right] I_\nu\right\} \\
&- \frac{\partial}{\partial \varepsilon}\left\{\varepsilon\left[(1-\mu^2)\frac{v}{cr} + \frac{\mu^2}{c}\frac{\partial v}{\partial r}\right] I_\nu\right\} \\
&+ \left[(3-\mu^2)\frac{v}{cr} + \frac{1+\mu^2}{c}\frac{\partial v}{\partial r}\right] I_\nu + \mathscr{A}_\nu \\
&= \eta_\nu - \chi_\nu I_\nu + \frac{\kappa_s}{4\pi}\int \Phi(\boldsymbol{\Omega}, \boldsymbol{\Omega}') I_\nu(\boldsymbol{\Omega}') d\boldsymbol{\Omega}' ,
\end{aligned} \tag{2}$$

where

$$\mathscr{A}_\nu = \frac{a}{c^2}\left[3\mu - (1-\mu^2)\frac{\partial}{\partial \mu} - \varepsilon\frac{\partial}{\partial \varepsilon}\right] I_\nu , \tag{3}$$

a is the matter acceleration, $\mu = \cos\theta$, ε is the neutrino energy, and η_ν is the emissivity of the medium. The subscript ν indicates neutrino energy dependence, and Φ is an angular phase function for neutrino scattering into the beam. This equation, good to $O(v/c)$ (where v is the matter velocity and c is the speed of light), assumes azimuthal symmetry and contains the appropriate redshift, aberration, and advection terms due to matter motion, angular redistribution due to scattering into the beam, scattering and absorption out of the beam, and source terms. Equation (2) does not include energy redistribution upon scattering, to be incorporated in a later version of the code. The various terms represent the additions and subtractions from the beam, the entire equation representing conservation of energy and number. The microphysics and collision terms reside on the right-hand side and the geometry; aberration, advection, and Doppler shift terms reside on the left.

While equation (2) contains the relevant terms to $O(v/c)$, it is a bit awkward to difference. It is also a bit ugly, and its various terms are not so cleanly distinguished by their physical roles. Dropping the acceleration term, we follow Eastman & Pinto (1993) and derive the form of the transport equation we employ in this study. The equation, physically equivalent to the Boltzmann equation (ignoring gravitational redshifts and the acceleration term) for an individual neutrino species, is

$$\begin{aligned}
\frac{1}{c}\frac{DI_\nu}{Dt} &+ \mu\frac{\partial I_\nu}{\partial r} + \frac{1-\mu^2}{r}(1-\beta Q\mu)\frac{\partial I_\nu}{\partial \mu} \\
&+ \frac{\beta}{r}(1+Q\mu^2)\left(3 - \frac{\partial}{\partial \ln \varepsilon}\right) I_\nu \\
&= \eta_\nu - \chi_\nu I_\nu + \frac{\kappa_s}{4\pi}\int \Phi(\boldsymbol{\Omega}, \boldsymbol{\Omega}') I_\nu(\boldsymbol{\Omega}') d\boldsymbol{\Omega}' ,
\end{aligned} \tag{4}$$

where $Q \equiv \partial \ln v/\partial \ln r - 1$ and all other symbols have their standard meanings. Φ is a phase function for neutrino scattering into the beam. χ_ν is the total extinction coefficient ($=\kappa_a + \kappa_s$), where κ_a and κ_s contain contributions from all absorption and scattering processes, respectively:

$$\kappa_s = \sum_i n_i \sigma_i^s \quad \text{and} \quad \kappa_a = \sum_i n_i \sigma_i^a . \tag{5}$$

Equation (4) can be rewritten as the corresponding Boltzmann equation for $\mathscr{F}_\nu$:

$$\begin{aligned}
\frac{1}{c}\frac{D\mathscr{F}_\nu}{Dt} &+ \mu\frac{\partial \mathscr{F}_\nu}{\partial r} + \frac{1-\mu^2}{r}(1-\beta Q\mu)\frac{\partial \mathscr{F}_\nu}{\partial \mu} \\
&- \frac{\beta}{r}(1+Q\mu^2)\frac{\partial \mathscr{F}_\nu}{\partial \ln \varepsilon} \\
&= \frac{h^3 c^2}{g}\left(\frac{\eta_\nu}{\varepsilon^3}\right) - \chi_\nu \mathscr{F}_\nu + \frac{\kappa_s}{4\pi}\int \Phi(\boldsymbol{\Omega}, \boldsymbol{\Omega}') \mathscr{F}_\nu(\boldsymbol{\Omega}') d\boldsymbol{\Omega}' ,
\end{aligned} \tag{6}$$

which can be mapped directly, term by term, into the Boltzmann equation employed by Messer et al. (1998) in their recent work on Boltzmann neutrino transfer. Equation (6) is the most useful form of the transport equation when studying it using the method of characteristics.

For neutrinos, the phase function for a scattering process i is well approximated (except for ν-e^- scattering) by

$$\Phi_i(\boldsymbol{\Omega}, \boldsymbol{\Omega}') = \Phi_i(\boldsymbol{\Omega} \cdot \boldsymbol{\Omega}') = (1 + \delta_i \boldsymbol{\Omega} \cdot \boldsymbol{\Omega}') = (1 + \delta_i \mu) , \tag{7}$$

where δ_i is a constant specific to each scattering process and μ is the angle between the incident and outgoing neutrinos. Hence, we can write the differential cross section for a scattering process i in terms of the total scattering cross section:

$$\frac{d\sigma_i^s}{d\Omega} = \frac{\sigma_i^s}{4\pi}(1 + \delta_i \mu) . \tag{8}$$

Subsequently, we drop the superscript s. Equation (7) implies that the angular redistribution term in equation (4) becomes

$$\kappa_s J_\nu + \frac{\kappa_s \delta_T}{4\pi} \boldsymbol{\Omega} \cdot \boldsymbol{F}_\nu , \tag{9}$$

where

$$\delta_T = \frac{\sum_i n_i \sigma_i \delta_i}{\sum_i n_i \sigma_i} . \tag{10}$$

F_ν in equation (9) is the neutrino flux, and J_ν is the zeroth moment defined by

$$J_\nu = \frac{1}{2}\int_{-1}^{1} I_\nu d\mu = \frac{c}{4\pi} E_\nu , \tag{11}$$

where E_ν is the neutrino energy density.

Integrating equation (4) and $\boldsymbol{\Omega}$ times equation (4) over $d\boldsymbol{\Omega}$ yields the zeroth and first moment equations, respectively:

$$\frac{1}{c}\frac{DJ_\nu}{Dt}+\frac{1}{r^2}\frac{\partial}{\partial r}(r^2H_\nu)-\frac{\beta Q}{r}(3P_\nu-J_\nu)+\frac{\beta}{r}\left(3-\frac{\partial}{\partial\ln\varepsilon}\right)(J_\nu+QP_\nu)=\kappa_a^*(B_\nu-J_\nu) \quad (12)$$

and

$$\begin{aligned}\frac{1}{c}\frac{DH_\nu}{Dt}&+\frac{\partial P_\nu}{\partial r}+\frac{3P_\nu-J_\nu}{r}-\frac{\beta Q}{r}(4N_\nu-2H_\nu)+\frac{\beta}{r}\left(3-\frac{\partial}{\partial\ln\varepsilon}\right)(H_\nu+QN_\nu)\\&=-\left(\kappa_a^*+\kappa_s-\frac{1}{3}\kappa_s\delta_T\right)H_\nu\\&=-(\kappa_a^*+\kappa_{\rm tr})H_\nu\,,\end{aligned} \quad (13)$$

where H_ν, P_ν, and N_ν are the first, second, and third angular moments given by

$$H_\nu=\frac{1}{2}\int_{-1}^{1}\mu I_\nu\,d\mu=\frac{1}{4\pi}F_\nu\,, \quad (14)$$

$$P_\nu=\tfrac{1}{2}\int_{-1}^{1}\mu^2 I_\nu\,d\mu\,, \quad (15)$$

and

$$N_\nu=\tfrac{1}{2}\int_{-1}^{1}\mu^3 I_\nu\,d\mu\,. \quad (16)$$

B_ν is the equilibrium (blackbody) spectral energy density times $c/(4\pi)$ and κ_a^* includes the correction for stimulated absorption (see § 5). $\kappa_{\rm tr}$ in equation (13) is the total transport extinction coefficient and is defined in terms of the individual transport cross sections as $\kappa_{\rm tr}=\sum_i n_i\sigma_i^{\rm tr}$. For a particular scattering process i,

$$\sigma_i^{\rm tr}=\int\frac{d\sigma_i}{d\Omega}(1-\mu)d\Omega=\sigma_i\left(1-\frac{1}{3}\delta_i\right). \quad (17)$$

Note that δ_p and δ_n, the δ_i for neutrino-nucleon scattering, are negative ($\delta_p\sim-0.2$ and $\delta_n\sim-0.1$) and, hence, that these processes are backward peaked. The fact that δ_p and δ_n are negative and, as a consequence, that $\sigma_i^{\rm tr}$ is greater than σ_i increases the neutrino-matter energy coupling rate for a given neutrino flux in the semitransparent region. This increase in inverse flux factor (J_ν/H_ν) is but one effect that can be studied with the transport tools we have developed and are developing.

Integrating equation (12) over energy, we obtain the neutrino energy equation:

$$\frac{DE}{Dt}+\frac{1}{r^2}\frac{\partial}{\partial r}(r^2F)-\frac{v}{r}(3p-1)QE+4\frac{v}{r}(1+Qp)E=4\pi\int_0^\infty\kappa_a^*(B_\nu-J_\nu)d\varepsilon\,, \quad (18)$$

where E and F are the integrated neutrino energy density and flux, respectively. p is the energy integrated Eddington factor, where $p_\nu=P_\nu/J_\nu$. The sums for all neutrino species of the negative of the right-hand side of equation (18) and the negative of the ε_ν integral of the right-hand side of equation (13) are the energy and momentum source terms in the matter equations. The two equations for the rate of change of the electron fraction (Y_e) due to $e^-/e^+/\nu_e/\bar\nu_e$ capture are

$$\rho\mathcal{N}_{\mathcal{A}}\frac{DY_e}{Dt_\pm}=\pm4\pi\int_0^\infty\kappa_a^*(B_\nu-J_\nu)_\pm\frac{d\varepsilon}{\varepsilon}\,, \quad (19)$$

where the minus sign is for the ν_e equation and the plus sign is for the $\bar\nu_e$ equation. Equations (4), (12), and (13) for each neutrino species, along with equation (19), are the basic neutrino transport equations that we solve. ρ is the mass density and $\mathcal{N}_{\mathcal{A}}$ is Avogadro's number.

3. METHOD OF SOLUTION: FEAUTRIER AND TANGENT-RAY ALGORITHM

We solve the moment equations (12) and (13) implicitly for J_ν and H_ν by backward differencing in time the quantities $J_\nu/\rho^{4/3}$ and $H_\nu/\rho^{2/3}$, backward differencing in $\ln\varepsilon$ (according to the slope of the characteristic), and combining the spatially differenced equations into one equation for J_ν that is second-order accurate in r. Standard matrix inversion techniques are employed to obtain J_ν, from which H_ν is derived using equation (13). This equation is manifestly Lagrangian and by solving it the advective derivative is included automatically. $J_\nu/\rho^{4/3}$ and $H_\nu/\rho^{2/3}$ are the natural combinations for adiabatic compression or expansion of a relativistic gas.

Since equations (12) and (13) contain the higher order angular moments P_ν and N_ν, closure relations are needed. These are obtained from a formal integration of the full transport equation (4), written in terms of the Feautrier variables:

$$U_\nu(\mu)=\tfrac{1}{2}[I_\nu(\mu)+I_\nu(-\mu)]$$

and

$$V_\nu(\mu)=\tfrac{1}{2}[I_\nu(\mu)-I_\nu(-\mu)]\,, \quad (20)$$

where μ ranges from 0 to 1.

In the isotropic scattering limit ($\delta_T=0$), these equations for U_ν and V_ν are

$$\frac{1}{c}\frac{DU_\nu}{Dt}+\mu\frac{\partial V_\nu}{\partial r}-\frac{1-\mu^2}{r}\beta Q\mu\frac{\partial U_\nu}{\partial\mu}+\frac{\beta}{r}\left(3-\frac{\partial}{\partial\ln\varepsilon}\right)(1+Q\mu^2)U_\nu=\eta_\nu-\chi_\nu U_\nu+\kappa_s J_\nu \quad (21)$$

and

$$\frac{1}{c}\frac{DV_\nu}{Dt}+\mu\frac{\partial U_\nu}{\partial r}-\frac{1-\mu^2}{r}\beta Q\mu\frac{\partial V_\nu}{\partial\mu}+\frac{\beta}{r}\left(3-\frac{\partial}{\partial\ln\varepsilon}\right)(1+Q\mu^2)V_\nu=-\chi_\nu V_\nu\,. \quad (22)$$

From the solution of equations (21) and (22), we obtain the full radiation field and the higher order moments that are then used in equations (12) and (13) for J_ν and H_ν. Since equations (21) and (22) require the lower order moment J_ν (and in principle H_ν; cf. eq. [9]), we iterate this system until we obtain a converged and consistent global solution.

Simultaneously, we calculate the Λ operator that maps S_ν, the source function, onto J_ν and employ accelerated Λ iteration (Cannon 1973a, 1973b; Scharmer 1981; Olson, Auer, & Buchler 1986; Eastman & Pinto 1993) to speed the convergence of the temperature and composition updates. Independent of the total optical depth, this generally requires no more than two to three iterations to obtain an accuracy of a part in 10^6. To maintain stability and reflect the density character of $U_\nu(\mu)$ and the flux character of $V_\nu(\mu)$, we stagger the $U_\nu(\mu)$ and $V_\nu(\mu)$ meshes with respect to one another by one-half a zone.

It may seem that by solving the moment equations separately and iterating with the solution of the transport equation itself and by not focusing simply on the solution of equations (21) and (22) or equation (4) that we are doing more than is necessary. An advantage of solving the moment equations is that they can be differenced to automatically conserve energy. However, enforcing energy conservation by construction does not guarantee that the solution obtained is the correct one. In fact, it is standard with many "nonconservative" hydrodynamic codes that do not difference the equations to conserve energy by construction to employ the degree to which energy is in fact conserved with time to assess their accuracy. We have chosen to retain the automatic energy-conserving feature, but in dynamical calculations we use electron lepton number conservation the global code check. By not differencing the equations to automatically conserve lepton number, since the equations we difference certainly do conserve lepton number, this is a useful approach. This is akin to employing entropy conservation in adiabatic flow as a check of a hydro code that is forced to conserve energy automatically by the particular differencing scheme employed. However, for the stationary atmospheres calculations we present here, for which the time derivative is zero, this is a moot point.

The advantage of calculating U_ν and V_ν instead of I_ν is that equations (21) and (22) can be differenced in such a way that V_ν will go accurately to $3\mu\,\partial S_\nu/\partial\tau_\nu$ in the large optical depth, diffusion limit, and still remain accurate in the optically thin, free-streaming limit. Schemes based directly on equation (2) or equation (4) have the correct large optical depth behavior for U_ν, i.e., $U_\nu = S_\nu$, but have round-off trouble computing V_ν, which is important if the only estimate of the flux comes from integrating μV_ν over angle (Larson, Morel, & Miller 1987). Typically in such codes above a certain optical depth the diffusion limit is assumed and V_ν is set equal to $3\mu\,\partial S_\nu/\partial\tau_\nu$.

Numerical methods that solve for the spatial variation of a specific-intensity–like variable (e.g., $I[\mu, r, E, t]$), such as all discrete ordinate transport methods, suffer from the problem that at large optical depth, the flux is not well determined (Morel, Wareing, & Smith 1996). This is a well-known problem, and the principle motivation for switching to Feautrier variables and to full range moment methods, in which J and H are solved for directly. Any S_N method has a spatial truncation error that is proportional to $(\Delta\tau)^k$, where k depends on the spatial discretization scheme. As $\Delta\tau$ grows, the error in the flux, which is proportional to $(\Delta\tau)^k$, also grows. For Feautrier variables, on the other hand, finite difference systems of equations that are at least second-order accurate in τ can be derived. These give an accurate representation of the radiation field in the free streaming limit and go naturally over to the diffusion limit when $\Delta\tau$ is large.

To solve equations (21) and (22), we employ the tangent-ray method (Schinder & Bludman 1989; Mihalas & Mihalas 1984). At a reference radial zone, tangents are constructed to each of the interior zones. The angles of the tangent rays to the normal at the reference zone define the angular grid at that zone on which the angular integrations are performed. Equations (21) and (22) are integrated along each tangent ray. If there are nx radial zones, the radiation field at the outer zone is resolved with $nx - 1$ angles; as you move inward the number of angles employed decreases linearly. Hence, if there are 100 radial zones, there are as many as 99 angular bins. With reasonable radial gridding, this approach can provide exquisite angular resolution, particularly for forward-peaked radiation fields, but at the cost of increased computational overhead. For instance, we have tested our implementation of the tangent-ray method with the Kosirev (1934) (spherical Milne) problem for which the absorptive opacity is assumed to be a power law in radius ($\kappa = 1/r^n$). For a variety of integer power laws (e.g., $n = 1.1$, 1.3, 1.5, 2, 3, 4), with from 100 to 500 radial zones, the tangent-ray method is superior to many implementations of the discrete ordinate method (Schinder & Bludman 1989). However, care must be taken to avoid purely geometrical zoning, for which $r_{n+1} = \alpha r_n$, since such zoning biases the angular binning in a systematic way. The result can be that the Eddington and flux factors asymptote at infinity to between 0.96 and 0.98, and not to 1.0. However, purely geometrical zoning is easily avoided in real calculations. Note that the increase in angular resolution with radius, which comes naturally from this procedure, is quite appropriate to spherical symmetry. Note also that the tangent-ray method is in some sense automatically adaptive for moving grids. At $r = 0$, the radiation field is by definition symmetric and needs no angular resolution. As r becomes large, a small bright central source is increasingly finely resolved.

For dynamical, time-dependent calculations, solving equations (21) and (22) by the tangent-ray method at each time step can be time consuming, but manageable. Fortunately, as long as the second and third angular moments do not change quickly, one need not solve equations (21) and (22) at every time step. Frequently, the solution to the moment equations (12) and (13) with previous values of p_ν and g_ν $(= N_\nu/H_\nu)$ can be quite accurate. In fact, this is most often the case, since the neutrino radiation fields rarely change on timescales shorter than $\sim$0.1 ms, whereas, because of the explicit nature of the hydro portion of the code, the Courant time steps are often near 1 μs. Hence, during much of the preexplosion delay and proto–neutron star phases, as well as during much of the core collapse phase, it is quite legitimate to solve for the Eddington factors only every few steps. An exception is during very dynamical phases such as shock breakout through the neutrinospheres.

Currently, there are two approximations in our algorithm for solving the transport equations (21) and (22). The first is that in calculating the radiation angular moments we assume that scattering into the beam is isotropic, while maintaining the correct transport cross section in the H_ν moment equation (13). To approximately incorporate the effects of anisotropic scattering, we employ the transport cross sections, as described and discussed above. Straightforward methods for solving the fully anisotropic problem using the Feautrier variables and the approaches outlined in this paper will be described elsewhere. The second approximation involves the assumption of linearity of the characteristics. The second term in both equations (21) and (22), which is proportional to $\partial/\partial\mu$, comes from the aberration experienced in going from the local to a nearby rest frame. The characteristics are not perfectly straight, which can make the calculation more difficult. One cannot simply integrate along a straight line impact ray. However, these terms are often insignificant because we require only an estimate of U_ν and V_ν and are using them to compute only the closure coefficients, p_ν and g_ν. Rather than just ignore these two terms, we have substituted

$$\frac{1-\mu^2}{r}\,\beta Q\mu\,\frac{\partial U_\nu}{\partial\mu}\rightarrow\frac{3\mu^2-1}{r}\,\beta Q U_\nu \tag{23}$$

in equation (21) and

$$\frac{1-\mu^2}{r}\,\beta Q\mu\,\frac{\partial V_\nu}{\partial\mu}\rightarrow\frac{4\mu^2-2}{r}\,\beta Q\mu V_\nu \tag{24}$$

in equation (22). The substitution in equation (23) is derived by integrating the left-hand side by parts, and the substitution in equation (24) is derived by integrating μ times the left-hand side by parts. Importantly, the two terms in equation (23) integrate to the same thing and μ times the two terms in equation (24) integrate to the same thing. Therefore, both modified equations reduce to the energy and momentum conservation equations.

In sum, we solve two coupled moment equations for the mean intensity and flux of the radiation field. These are the fundamental results of the transport calculation. They are solved by an Eddington factor iteration wherein a set of angle-dependent equations consistent with the moment equations are solved for the intensity given a constant source function, and this intensity is used to determine the closure factors in the moment solution.

4. IMPLICIT COUPLING TO MATTER AND ACCELERATED Λ ITERATION

Though we are not highlighting in this paper time-dependent calculations, we think it useful to include a discussion of the technique we employ to couple matter with neutrinos. This is done implicitly in operator-split fashion, after each hydro update. For each neutrino species, the scattering and absorption opacities and the emissivities are calculated and fed into the transport solver. A fully converged solution of the transport equations is obtained and this is used to calculate the various terms needed for the implicit update of the temperature and Y_e because of transport. In particular, the derivatives with respect to temperature and Y_e of the right-hand sides of equations (18) and (19) are calculated. For the implicit temperature update at each radial zone, i, a backward-differenced matter energy equation such as

$$\rho C_V\,\frac{T_i^{k+1}-T_i^k+\Delta T_i}{\Delta t}=-4\pi\int_0^\infty(\eta'-\kappa_a^* J_\nu)d\varepsilon - 4\pi\,\Delta T_i\int_0^\infty\left(\frac{\partial\eta'}{\partial T}-\frac{\partial\kappa_a^*}{\partial T}\,J_\nu-\kappa_a^*\,\frac{\partial J_\nu}{\partial T}\right)d\varepsilon \tag{25}$$

is constructed, where ΔT_i is the temperature change between iterations, T_i^{k+1} is the new temperature, T_i^k is the old temperature, C_V is the specific heat, η' is not corrected for final-state neutrino blocking (§ 5), and Δt is the time step. (In fact, the matter energy is a function of both T and Y_e, and there is an extra term in the temperature update equation to account for the entropy change because of the Y_e composition change. That term has been dropped here for clarity, but not in the computations.)

The subtlety with equation (25) lies in the $\partial J_\nu/\partial T$ term. In general, J_i equals $\Lambda_{ij}S_j$ at each frequency or energy, where the Λ operator is a matrix coupling different zones. Hence, equation (25) is a matrix equation with

$$\frac{\partial J_i}{\partial T}=\Lambda_{ij}\,\frac{\partial S_j}{\partial T}\,. \tag{26}$$

For simplicity in equation (25), we have dropped in equation (26) the Γ operator that couples energy groups. Though we have the option in the code of calculating the full Λ matrix, we use only the diagonal and the two adjacent off diagonals. It is this truncated tridiagonal Λ operator that we actually employ.

Since the S_ν we use in equation (26), perhaps a bit idiosyncratically, equals η'/κ^*, $\partial S/\partial T$ is given by

$$\frac{\partial S_i}{\partial T}=\left(\frac{\partial\eta_i'}{\partial T}-S_i\,\frac{\partial\kappa_i^*}{\partial T}\right)\Big/\kappa_i^*\,, \tag{27}$$

and this is employed to derive

$$\frac{\partial J_i}{\partial T}=\Lambda_{i,i+1}\,\frac{\partial S_{i+1}}{\partial T}+\Lambda_{i,i-1}\,\frac{\partial S_{i-1}}{\partial T}+\Lambda_{i,i}\,\frac{\partial S_i}{\partial T}\,. \tag{28}$$

Plugging equation (28) into equation (25), we solve for ΔT_i by inverting the tridiagonal matrix. For the ν_e and $\bar\nu_e$ species, a similar procedure is followed to obtain ΔY_e from equation (19). Note that the integral over neutrino energy is performed before the T and Y_e updates, which are not attempted for each energy group individually.

Once ΔT_i and ΔY_e^i are obtained, T_i^{k+1} is set equal to $T_i^k+\Delta T_i$ and $Y_e^{k+1,i}$ is set equal to $Y_e^{k,i}+\Delta Y_e^i$. We then loop back to obtain a new transport solution with the new temperature and Y_e. This procedure is iterated until $\Delta T_i/T_i$ and $\Delta Y_e^i/Y_e^i$ are suitably small (normally 10^{-6}) for all zones, at which time we are left with a completely consistent set of J_ν, H_ν, U_ν, V_ν, T, and Y_e. T_i^k and Y_e^i are not changed during the iteration. The total number of iterations varies between 1 and 7, the latter only when Y_e is changing fast in either the ν_e or the $\bar\nu_e$ modules. The various neutrino fluids are updated in series, not in parallel, and we generally follow three species: ν_e, $\bar\nu_e$, and "ν_μ," the latter representing the sum of ν_μ, $\bar\nu_\mu$, ν_τ, and $\bar\nu_\tau$ neutrinos. Bunching these four neutrino species into one assumes that their cross sections and source terms are identical, which technically is false, but quantitatively reasonable. Note that to achieve stable iteration, it is essential for the derivatives in equation (25) to be accurate. Among other things, this requires good derivatives of $\hat\mu$ $(=\mu_n-\mu_p)$ with respect to T and Y_e. Analytic derivatives are preferred, but numerical derivatives for most quantities seem to work.

As stated previously, to achieve rapid convergence of the transport iteration we employ accelerated Λ iteration (ALI; Cannon 1973a, 1973b; Scharmer 1981; Olson et al. 1986). This entails an approximation that improves during the iteration. In particular, we use

$$J_\nu^{k+1}=J_\nu^k+\Lambda^k(S_\nu^{k+1}-S_\nu^k)\,, \tag{29}$$

where Λ^k is the retarded Λ operator. We use only its diagonal and first off-diagonal terms. This procedure accelerates and stabilizes the iteration, even if the optical depth is large and the scattering albedo is high. Note that one cannot iterate on the full Λ matrix (the inverse of the matrix representation of the finite-difference transport equations) because its eigenvalues are very close to the unit circle and the iteration stabilizes instead of converging. Subtracting off a piece of the Λ matrix and lagging the iteration of that piece allows the iteration to converge much more rapidly.

5. STIMULATED ABSORPTION

The concept of stimulated emission for photons is well understood and studied, but the corresponding concept of stimulated *absorption* for neutrinos is not so well appreciated. This may be because its simple origin in Fermi blocking and the Pauli exclusion principle in the context of *net* emission is not often explained. The *net* emission of a neutrino is simply the difference between the emissivity and the absorption of the medium:

$$\mathscr{I}_{\rm net} = \eta_\nu - \kappa_a I_\nu \, . \tag{30}$$

All absorption processes involving fermions will be inhibited by Pauli blocking due to final-state occupancy. Hence, η_ν in equations (30) and (4) includes a blocking term, $(1 - \mathscr{F}_\nu)$ (Bruenn 1985). $\mathscr{F}_\nu$ is the invariant distribution function for the neutrino, whether or not it is in chemical equilibrium.

We can derive stimulated absorption using Fermi's Golden rule. For example, the net collision term for the process, $\nu_e n \leftrightarrow e^- p$, is

$$\begin{aligned}\mathscr{C}_{\nu_e n \leftrightarrow e^- p} = & \int \frac{d^3 \boldsymbol{p}_{\nu_e}}{(2\pi)^3} \int \frac{d^3 \boldsymbol{p}_n}{(2\pi)^3} \int \frac{d^3 \boldsymbol{p}_p}{(2\pi)^3} \\ & \times \int \frac{d^3 \boldsymbol{p}_e}{(2\pi)^3} \left(\sum_s |\mathscr{M}|^2 \right) \Xi(\nu_e n \leftrightarrow e^- p)(2\pi)^4 \delta^4 \\ & \times (\mathbf{p}_{\nu_e} + \mathbf{p}_n - \mathbf{p}_p - \mathbf{p}_e) \, ,\end{aligned} \tag{31}$$

where $\mathbf{p}$ is a four-vector and

$$\begin{aligned}\Xi(\nu_e n \leftrightarrow e^- p) = & \mathscr{F}_{\nu_e} \mathscr{F}_n (1 - \mathscr{F}_e)(1 - \mathscr{F}_p) \\ & - \mathscr{F}_e \mathscr{F}_p (1 - \mathscr{F}_n)(1 - \mathscr{F}_{\nu_e}) \, .\end{aligned} \tag{32}$$

The final-state blocking terms in equation (32) are manifest, in particular that for the ν_e neutrino. Algebraic manipulations convert $\Xi(\nu_e n \leftrightarrow e^- p)$ in equation (32) into

$$\begin{aligned}\Xi(\nu_e n \leftrightarrow e^- p) = & \mathscr{F}_n (1 - \mathscr{F}_e)(1 - \mathscr{F}_p) \\ & \times \left[\frac{\mathscr{F}'_{\nu_e}}{1 - \mathscr{F}'_{\nu_e}} (1 - \mathscr{F}_{\nu_e}) - \mathscr{F}_{\nu_e} \right] \\ = & \frac{\mathscr{F}_n (1 - \mathscr{F}_e)(1 - \mathscr{F}_p)}{1 - \mathscr{F}'_{\nu_e}} (\mathscr{F}'_{\nu_e} - \mathscr{F}_{\nu_e}) \, ,\end{aligned} \tag{33}$$

where

$$\mathscr{F}'_{\nu_e} = (e^{[\varepsilon_{\nu_e} - (\mu_e - \hat{\mu})]\beta} + 1)^{-1} \tag{34}$$

is an equilibrium distribution function for the ν_e neutrino and it has been assumed that only the electron, proton, and neutron are in thermal equilibrium. Note that in $\mathscr{F}'_{\nu_e}$ there is no explicit reference to a neutrino chemical potential, though of course in beta equilibrium it is equal to $\mu_e - \hat{\mu}$. There is no need to construct or refer to a neutrino chemical potential in neutrino transfer.

Using equation (1), we see that equation (33) naturally leads to

$$\mathscr{I}_{\rm net} = \frac{\kappa_a}{1 - \mathscr{F}'_\nu} (B_\nu - I_\nu) = \kappa_a^* (B_\nu - I_\nu) \, . \tag{35}$$

This is akin to the right-hand side of equation (12). If neutrinos were bosons, we would have found a term $(1 + \mathscr{F}'_\nu)$ in the denominator, but the form of equation (35), in which I_ν is manifestly driven to B_ν, the equilibrium intensity, would have been retained. From equations (33) and (35), we see that the stimulated absorption correction to κ_a is $1/(1 - \mathscr{F}'_\nu)$. If we want to retain the form of the collision term as expressed in equations (30) or (4), the physics is unaltered and stimulated absorption is not needed as a concept, as long as η_ν in equation (4) contains the neutrino Pauli blocking term, $(1 - \mathscr{F}_\nu)$, without the prime. However, by writing the collision term in the form of equation (35), with κ_a corrected for stimulated absorption, we have a net source term that clearly drives I_ν to equilibrium. The timescale is $1/c\kappa_a^*$. Though the derivation of the stimulated absorption correction we have provided here is for the $\nu_e n \leftrightarrow e^- p$ process, this correction is quite general and applies to all neutrino absorption opacities.

Kirchhoff's Law, expressing detailed balance, is

$$\kappa_a = \eta_\nu / B_\nu \quad \text{or} \quad \kappa_a^* = \eta'_\nu / B_\nu \, , \tag{36}$$

where η'_ν is not corrected for final-state neutrino blocking. Furthermore, the net emissivity can be written as the sum of its *spontaneous* and *induced* components:

$$\eta_\nu = \kappa_a \left[\frac{B_\nu}{1 \pm \mathscr{F}'_\nu} + \left(1 - \frac{1}{1 \pm \mathscr{F}'_\nu} \right) I_\nu \right] , \tag{37}$$

where the plus or minus sign is used for bosons or fermions, respectively.

6. NEUTRINO CROSS SECTIONS

Neutrino-matter cross sections, both for scattering and for absorption, play the central role in neutrino transport. The major processes are the superallowed charged-current absorptions of ν_e and $\bar{\nu}_e$ neutrinos on free nucleons, neutral-current scattering off of free nucleons (Schinder 1990; Janka et al. 1996; Burrows & Sawyer 1998, 1999; Reddy, Prakash, & Lattimer 1998; Yamada 2000, in preparation), alpha particles, and nuclei (Freedman 1974; Leinson, Oraevsky, & Semikoz 1988; Horowitz 1997; Burrows, Mazurek, & Lattimer 1980), neutrino-electron/positron scattering (Schinder & Shapiro 1982a, 1982b, 1983), neutrino-nucleus absorption, neutrino-neutrino scattering, neutrino-antineutrino absorption (Janka 1991), and the inverses of various neutrino production processes such as nucleon-nucleon bremsstrahlung and the modified URCA process ($\nu_e + n + n \rightarrow e^- + p + n$). Compared with photon-matter interactions, neutrino-matter interactions are relatively simple functions of incident neutrino energy. Resonances play little or no role and continuum processes dominate. Nice summaries of the various neutrino cross sections of relevance in supernova theory are given in Tubbs & Schramm (1975) and in Bruenn (1985). In particular, Bruenn (1985) discusses in detail neutrino-electron scattering and neutrino-antineutrino processes (see also Dicus 1972) using the full energy redistribution formalism. He also provides a serviceable approximation to the neutrino-nucleus absorption cross section (Fuller 1982; Fuller, Fowler, & Newman 1980; Aufderheide et al. 1994). Recall that for a neutrino energy of ~ 10 MeV the ratio of the charged-current cross section to the ν_e-electron scattering cross section is ~ 100. However, neutrino-electron scattering does play a role, along with neutrino-nucleon scattering and nucleon-nucleon bremsstrahlung, in the energy equilibration of emergent ν_μ neutrinos, though the relative contribution of each has yet to be determined. In this context, our current lack of an energy redistribution algorithm should be borne in mind. Nevertheless, our general conclusions in § 10 concerning the ν_μ neutrinos, their softer than previously believed spectra, the likely role of bremsstrahlung in their production, and the consequences of their high scattering albedos, will be strengthened only when competent energy redistribution is included.

6.1. *Charged-Current Absorption*

The cross section per baryon for either ν_e or $\bar{\nu}_e$ absorption on free nucleons is larger than that for any other process. Given the large abundances of free neutrons and protons in proto–neutron star atmospheres, these processes are central to ν_e neutrino transport. A convenient reference neutrino cross section is σ_o, given by

$$\sigma_o = \frac{4G^2(m_e c^2)^2}{\pi(\hbar c)^4} \simeq 1.705 \times 10^{-44} \text{ cm}^2 . \tag{38}$$

The total $\nu_e + n \to e^- + p$ absorption cross section is then given by

$$\sigma^a_{\nu_e n} = \sigma_o \left(\frac{1+3g_A^2}{4}\right)\left(\frac{\varepsilon_{\nu_e} + \Delta_{np}}{m_e c^2}\right)^2 \times \left[1 - \left(\frac{m_e c^2}{\varepsilon_{\nu_e} + \Delta_{np}}\right)^2\right]^{1/2} W_M . \tag{39}$$

The corresponding absorption cross section for the process, $\bar{\nu}_e + p \to e^+ + n$, is

$$\sigma^a_{\bar{\nu}_e p} = \sigma_o \left(\frac{1+3g_A^2}{4}\right)\left(\frac{\varepsilon_{\bar{\nu}_e} - \Delta_{np}}{m_e c^2}\right)^2 \times \left[1 - \left(\frac{m_e c^2}{\varepsilon_{\bar{\nu}_e} - \Delta_{np}}\right)^2\right]^{1/2} W_{\bar{M}} . \tag{40}$$

g_A is the axial-vector coupling constant (~ -1.26) and $\Delta_{np} = m_n c^2 - m_p c^2 = 1.29332$ MeV. W_M is the correction for weak magnetism and recoil (Vogel 1984), never before included in supernova simulations, and is approximately equal to $(1 + 1.1\varepsilon_{\nu_e}/m_n c^2)$ for ν_e absorption on neutrons. At $\varepsilon_{\nu_e} = 20$ MeV, this correction is only $\sim 2.5\%$. The corresponding correction ($W_{\bar{M}}$) for $\bar{\nu}_e$ neutrino absorption on protons is $(1 - 7.1\varepsilon_{\bar{\nu}_e}/m_n c^2)$, which at 20 MeV is a large -15%. To calculate κ^*_a, $\sigma^a_{\nu_e n}$ and $\sigma^a_{\bar{\nu}_e p}$ must be multiplied by the appropriate stimulated absorption correction, $1/(1 - \mathscr{F}'_{\nu_e})$ or $1/(1 - \mathscr{F}'_{\bar{\nu}_e})$. Furthermore, final-state blocking by either electrons or positrons and either protons or neutrons (à la eq. [33]) must be included. The consequences of these various terms for the neutrino spectra and neutrino-matter heating rates are explored in § 8. Note that the sign of $\mu_e - \hat{\mu}$ in the stimulated absorption correction for $\bar{\nu}_e$ neutrinos is flipped, as is the sign of μ_e in the positron blocking term. Note also that the $\bar{\nu}_e + p \to e^+ + n$ process dominates the supernova neutrino signal in proton-rich underground neutrino telescopes on Earth, such as Super Kamiokande, LVD, and MACRO, a fact that emphasizes the interesting complementarities between emission at the supernova and detection in Cerenkov and scintillation facilities.

7. NUCLEON-NUCLEON BREMSSTRAHLUNG

A production process for neutrino/antineutrino pairs that has received but little attention to date in the supernova context is neutral-current nucleon-nucleon bremsstrahlung ($n_1 + n_2 \to n_3 + n_4 + \nu\bar{\nu}$). Its importance in the cooling of old neutron stars, for which the nucleons are quite degenerate, has been recognized for years (Flowers, Sutherland, & Bond 1975), but only in the last few years has it been studied for its potential importance in the atmospheres of protoneutron stars and supernovae (Suzuki 1993; Burrows 2000; Hannestad & Raffelt 1998). As a consequence, it has never before been incorporated into supernova codes. Neutron-neutron, proton-proton, and neutron-proton bremsstrahlung are all important, with the latter the most important for symmetric matter. As a source of ν_e and $\bar{\nu}_e$ neutrinos, nucleon-nucleon bremsstrahlung can not compete with the charged-current capture processes. However, for a range of temperatures and densities realized in supernova cores, it may compete with e^+e^- annihilation as a source for ν_μ, $\bar{\nu}_\mu$, ν_τ, and $\bar{\nu}_\tau$ neutrinos ("ν_μ"). The major obstacles to obtaining accurate estimates of the emissivity of this process are our poor knowledge of the nucleon-nucleon potential, of the degree of suitability of the Born Approximation, and of the magnitude of many-body effects (Hannestad & Raffelt 1998; Raffelt & Seckel 1991; Brinkman & Turner 1988). Since the nucleons in protoneutron star atmospheres are not degenerate, we present here a calculation of the total and differential emissivities of this process in that limit and assume a one-pion exchange (OPE) potential model to calculate the nuclear matrix element. To acknowledge ignorance, we encourage that a fudge factor of order unity, but perhaps as low as 0.1, be appended to the rate. The formalism we employ has been heavily influenced by those of Brinkman & Turner (1988) and Hannestad & Raffelt (1998), to which the reader is referred for details and further explanations.

Our focus is on obtaining a useful single-neutrino final-state emission (source) spectrum, as well as a final-state pair energy spectrum and the total emission rate. For this, we start with Fermi's Golden Rule for the total rate per neutrino species:

$$Q_{nb} = (2\pi)^4 \int \left[\prod_{i=1}^{4} \frac{d^3\boldsymbol{p}_i}{(2\pi)^3}\right] \frac{d^3\boldsymbol{q}_\nu}{(2\pi)^3 2\omega_\nu} \frac{d^3\boldsymbol{q}_{\bar{\nu}}}{(2\pi)^3 2\omega_{\bar{\nu}}} \times \omega \sum_s |\mathscr{M}|^2 \delta^4(\mathbf{P}) \mathscr{F}_1 \mathscr{F}_2 (1 - \mathscr{F}_3)(1 - \mathscr{F}_4) , \tag{41}$$

where $\delta^4(\mathbf{P})$ is four-momentum conservation delta function, ω is the energy of the final-state neutrino pair, $(\omega_\nu, \boldsymbol{q}_\nu)$ and $(\omega_{\bar{\nu}}, \boldsymbol{q}_{\bar{\nu}})$ are the energy and momentum of the neutrino and antineutrino, respectively, and $\boldsymbol{p}_i$ is the momentum of nucleon i. Final-state neutrino and antineutrino blocking have been dropped.

The necessary ingredients for the integration of equation (41) are the matrix element for the interaction and a workable procedure for handling the phase space terms, constrained by the conservation laws. We follow Brinkmann & Turner (1988) for both of these elements. In particular, we assume for the $n + n \to n + n + \nu\bar{\nu}$ process that the matrix element is

$$\sum_s |\mathscr{M}|^2 = (64/4)G^2(f/m_\pi)^4 g_A^2 \left[\left(\frac{k^2}{k^2 + m_\pi^2}\right)^2 + \cdots\right] \frac{\omega_\nu \omega_{\bar{\nu}}}{\omega^2}$$

$$= A\, \frac{\omega_\nu \omega_{\bar{\nu}}}{\omega^2}\,, \tag{42}$$

where the "4" in the denominator accounts for the spin average for identical nucleons, G is the weak coupling constant, $f\,(\sim 1.0)$ is the pion-nucleon coupling constant, g_A is the axial-vector coupling constant, the term in brackets is from the OPE propagator plus exchange and cross terms, k is the nucleon momentum transfer, and m_π is the pion mass. In equation (42), we have dropped $\boldsymbol{q}_\nu \cdot \boldsymbol{k}$ terms from the weak part of the total matrix element. To further simplify the calculation, we set the "propagator" term equal to a constant ζ, a number of order unity, and absorb into ζ all interaction ambiguities. The constant A in equation (42) remains.

Inserting a $\int \delta(\omega - \omega_\nu - \omega_{\bar{\nu}}) d\omega$ by the neutrino phase space terms times $\omega\omega_\nu\omega_{\bar{\nu}}/\omega^2$ and integrating over $\omega_{\bar{\nu}}$ yields

$$\int \omega\, \frac{\omega_\nu \omega_{\bar{\nu}}}{\omega^2}\, \frac{d^3\boldsymbol{q}_\nu}{(2\pi)^3 2\omega_\nu}\, \frac{d^3\boldsymbol{q}_{\bar{\nu}}}{(2\pi)^3 2\omega_{\bar{\nu}}}$$

$$\to \frac{1}{(2\pi)^4} \int_0^\infty \int_0^\omega \frac{\omega_\nu^2(\omega - \omega_\nu)^2}{\omega}\, d\omega_\nu\, d\omega\,, \tag{43}$$

where again ω equals $(\omega_\nu + \omega_{\bar{\nu}})$. If we integrate over ω_ν, we can derive the ω spectrum. A further integration over ω will result in the total volumetric energy emission rate. If we delay such an integration, after the nucleon phase space sector has been reduced to a function of ω and if we multiply equation (41) and/or equation (43) by ω_ν/ω, an integration over ω from ω_ν to infinity will leave the emission spectrum for the single final-state neutrino. This is of central use in multienergy group transport calculations and with this differential emissivity and Kirchhoff's Law (§ 5) we can derive an absorptive opacity.

Whatever our final goal, we need to reduce the nucleon phase space integrals and to do this we use the coordinates and approach of Brinkmann & Turner (1988). We define new momenta: $p_+ = (p_1 + p_2)/2$, $p_- = (p_1 - p_2)/2$, $p_{3c} = p_3 - p_+$, and $p_{4c} = p_4 - p_+$, where nucleons 1 and 2 are in the initial state. Useful direction cosines are $\gamma_1 = p_+ \cdot p_-/|p_+||p_-|$ and $\gamma_c = p_+ \cdot p_{3c}/|p_+||p_{3c}|$. Defining $u_i = p_i^2/2mT$ and using energy and momentum conservation, we can show that

$$\begin{aligned} d^3p_1\, d^3p_2 &= 8 d^3p_+\, d^3p_- \\ \omega &= 2T(u_- - u_{3c}) \\ u_{1,2} &= u_+ + u_- \pm 2(u_+ u_-)^{1/2}\gamma_1 \\ u_{3,4} &= u_+ + u_{3c} \pm 2(u_+ u_{3c})^{1/2}\gamma_c\,. \end{aligned} \tag{44}$$

In the nondegenerate limit, the $\mathscr{F}_1 \mathscr{F}_2(1 - \mathscr{F}_3)(1 - \mathscr{F}_4)$ term reduces to $e^{2y}e^{-2(u_+ + u_-)}$, where y is the nucleon degeneracy factor. Using equation (44), we see that the quantity $(u_+ + u_-)$ is independent of both γ_1 and γ_c. This is a great simplification and makes the angle integrations trivial. Annihilating d^3p_4 with the momentum delta function in equation (41), noting that $p_i^2\, dp = [(2mT)^{3/2}/2] u_i^{1/2}\, du_i$, pairing the remaining energy delta function with u_-, and integrating u_+ from 0 to ∞, we obtain

$$dQ_{nb} = \frac{Am^{4.5}}{2^8 \times 3 \times 5\pi^{8.5}}\, T^{7.5} e^{2y} e^{-\omega/T} (\omega/T)^4 \times \left[\int_0^\infty e^{-x}(x^2 + x\omega/T)^{1/2}\, dx\right] d\omega\,. \tag{45}$$

The variable x over which we are integrating in equation (45) is equal to $2u_{3c}$. That integral is analytic and yields

$$\int_0^\infty e^{-x}(x^2 + x\omega/T)^{1/2}\, dx = \eta e^\eta K_1(\eta)\,, \tag{46}$$

where K_1 is the standard modified Bessel function of imaginary argument, related to the Hankel functions, and $\eta = \omega/2T$. Hence, the ω spectrum is given by

$$\frac{dQ_{nb}}{d\omega} \propto e^{-\omega/2T}\omega^5 K_1(\omega/2T)\,. \tag{47}$$

It can easily be shown that $\langle\omega\rangle = 4.364T$ (Raffelt & Seckel 1991). Integrating equation (45) over ω and using the thermodynamic identity in the nondegenerate limit,

$$e^y = \left(\frac{2\pi}{mT}\right)^{3/2} n_n/2\,, \tag{48}$$

where n_n is the density of neutrons (in this case), we derive for the total neutron-neutron bremsstrahlung emissivity of a single neutrino pair

$$Q_{nb} = 1.04 \times 10^{30}\zeta(X_n\rho_{14})^2 \left(\frac{T}{\mathrm{MeV}}\right)^{5.5} \mathrm{ergs\ cm^{-3}\ s^{-1}}\,, \tag{49}$$

where ρ_{14} is the mass density in units of 10^{14} g cm^{-3} and X_n is the neutron mass fraction. Interestingly, this is within 30% of the result in Suzuki (1993), even though he has substituted, without much justification, $(1 + \omega/2T)$ for the integral in equation (45). $\{[1 + (\pi\eta/2)^{1/2}]$ is a better approximation.$\}$ The proton-proton and neutron-proton processes can be handled similarly, and the total bremsstrahlung rate is then obtained by substituting $X_n^2 + X_p^2 + (28/3)X_n X_p$ for X_n^2 in equation (49) (Brinkmann & Turner 1988). At $X_n = 0.7$, $X_p = 0.3$, $\rho = 10^{12}$ g cm^{-3}, and $T = 10$ MeV, and taking the ratio of augmented equation (49) to the total rate for e^+e^- production of $\nu_\mu\bar{\nu}_\mu$ pairs (Dicus 1972), we obtain the promising ratio of $\sim 5\zeta$. Setting the correction factor ζ equal to ~ 0.5 (Hannestad & Raffelt 1998), we find that, near and just deeper than the ν_μ neutrinosphere, the bremsstrahlung rate is larger than that for classical pair production.

If in equation (43) we do not integrate over ω_ν, but at the end of the calculation we integrate over ω from ω_ν to ∞, then after some manipulation we obtain the single neutrino emissivity spectrum:

$$\begin{aligned} \frac{dQ'_{nb}}{d\omega_\nu} &= 2C\left(\frac{Q_{nb}}{T^4}\right)\omega_\nu^3 \int_{\eta_\nu}^\infty \frac{e^{-\eta}}{\eta} K_1(\eta)(\eta - \eta_\nu^b)^2\, d\eta \\ &= 2C\left(\frac{Q_{nb}}{T^4}\right)\omega_\nu^3 \int_1^\infty \frac{e^{-2\eta_\nu^b\xi}}{\xi^3} (\xi^2 - \xi)^{1/2}\, d\xi\,, \end{aligned} \tag{50}$$

where $\eta_\nu^b = \omega_\nu/2T$, C is the normalization constant equal to $(3 \times 5 \times 7 \times 11)/2^{11}$ ($\cong 0.564$), and for the second expression we have used the integral representation of $K_1(\eta)$ and reversed the order of integration. In equation (50), Q_{nb} is the emissivity for the pair.

Equation (50) is the approximate neutrino emission spectrum due to nucleon-nucleon bremsstrahlung. A useful fit to equation (50), good to better than 3% over the full range of important values of η_ν, is

$$\frac{dQ'_{nb}}{d\omega_\nu} \cong \frac{0.234 Q_{nb}}{T} \left(\frac{\omega_\nu}{T}\right)^{2.4} e^{-1.1\omega_\nu/T} . \tag{51}$$

Setting ζ equal to 0.5, we have incorporated bremsstrahlung into our Feautrier transport algorithm. In § 10, we show how the emergent ν_μ spectrum depends upon ζ.

8. BASIC NEUTRINO TRANSPORT RESULTS

The formalism and microphysics described in §§ 2–7 were used to calculate the neutrino radiation fields for two snapshot profiles in temperature, density, electron fraction, and velocity. One of these is from the work of Burrows et al. (1995) and represents the wind phase that follows explosion (model W). The second profile (our model BM) was kindly provided to us by T. Mezzacappa and is from a multigroup, flux-limited diffusion simulation by Bruenn (Messer et al. 1998), 106 ms after the bounce of the core of the Weaver & Woosley (1995) 15 $M_\odot$ star. Since Messer et al. (1998) have already published their results for this model, in order to facilitate comparison we highlight our results for model BM. Note that our focus is on neutrino atmospheres and not on completely self-consistent profiles and their evolution. Hence, differences between the equations of state and microphysics employed in two different dynamical calculations, in particular any differences between the $\hat{\mu}$, will translate at a given epoch into differences in composition and thermal profiles. Postprocessing one group's snapshots with the code of another can lead to differences in the neutrino fields that are larger than the differences in their thermal profiles. The ν_e and $\bar{\nu}_e$ neutrino luminosity profiles and spectra are particularly sensitive to differences between the $\hat{\mu}$ used. To check this, after achieving a steady state we turned on the Y_e coupling for about 5 ms. The upshot was that Y_e changed very little, demonstrating that we were using substantially the same $\hat{\mu}$ as Messer et al. (1998).

We concentrate on the generic features of the energy, angle, and spatial distributions of the various neutrino radiation fields. We use 50 energy groups, concentrating them below 50 MeV, so that the emergent spectra are well resolved. The models have 120 spatial grid points out to a radius of about 300 km, and we interpolate in the various original models to resolve important features, such as the neutrinospheres and the shock wave (for model BM). Since we are using the tangent-ray method to set up and determine the angular grid, we employ from 119 to a few angular groups. In the code, we can establish an arbitrary number of "core rays" in the interior to increase the angular coverage at small radii, but we found that we did not need to exercise this option.

The temperature (T), density (ρ), and Y_e profiles for the two models are shown in Figure 1. Model BM is a preexplosion protoneutron star in a stalled shock configuration, while model W is a snapshot of a postexplosion neutrino-driven wind that expands off of the protoneutron star after

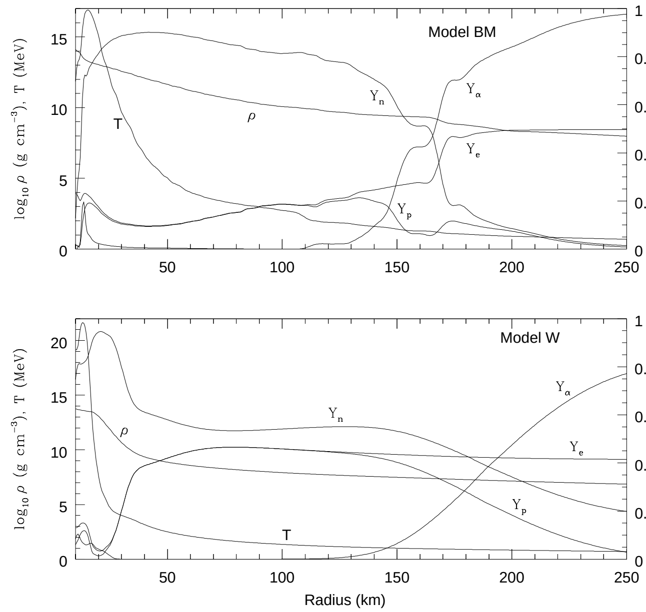

FIG. 1.—Temperature (T), density (ρ), electron fraction (Y_e), proton fraction (Y_p), neutron fraction (Y_n), and alpha fraction (Y_α) for models BM (*top panel*) and W (*bottom panel*). In model BM, the shock is located at 170 km, but in model W there is no shock on the grid.

explosion. In model W from Burrows et al. (1995), Y_e asymptotes to a value determined by the competition between ν_e and $\bar{\nu}_e$ neutrino absorption, e^- and e^+ capture on nucleons, and the speed of expansion. This situation is similar to that found in a gasdynamic laser or freeze out in the early universe. The actual asymptotic Y_e and acceleration timescale will depend, in a self-consistent calculation, on the details of the neutrino-matter coupling and radiation fields and will be the subject of a future paper. Also shown in the lower panel of Figure 1 are the neutron, proton, and alpha particle mass fractions that bear on the physics of wind acceleration and the viability of this wind as a site for the r-process (Woosley & Hoffman 1992; Qian & Woosley 1996).

8.1. *Optical Depths and Scattering Albedos versus Radius and Energy*

The integrated depth versus radius or interior mass provides a measure of the global context of any transport problem. Figure 2 shows the depth versus radius and neutrino energy for ν_e neutrinos with energies from 5 to 30 MeV in model BM. This is not the Rosseland mean, which, because of the much higher average neutrino energies in the deep interior, reaches a value greater than 10^5 at the center. The position of the shock wave is manifest. Figure 2 demonstrates that the position of the neutrinosphere ($\tau \sim \frac{2}{3}$) is a stiff function of neutrino energy. For ν_e neutrinos and the energies depicted in the figure, the radii of the neutrinospheres range from ~ 50 to ~ 130 km, more than a factor of 2. For the $\bar{\nu}_e$ and ν_μ neutrinos, the range is similarly broad, though because of the weaker neutrino-matter coupling for these neutrinos the radii are correspondingly smaller. These facts emphasize the dubious merit of referring to a single neutrinosphere for a given species. Figure 3 depicts the positions of the neutrinospheres versus energy and type. In model BM, while 10 MeV ν_e neutrinos decouple at ~ 80 km, 100 MeV neutrinos decouple as far out as the position

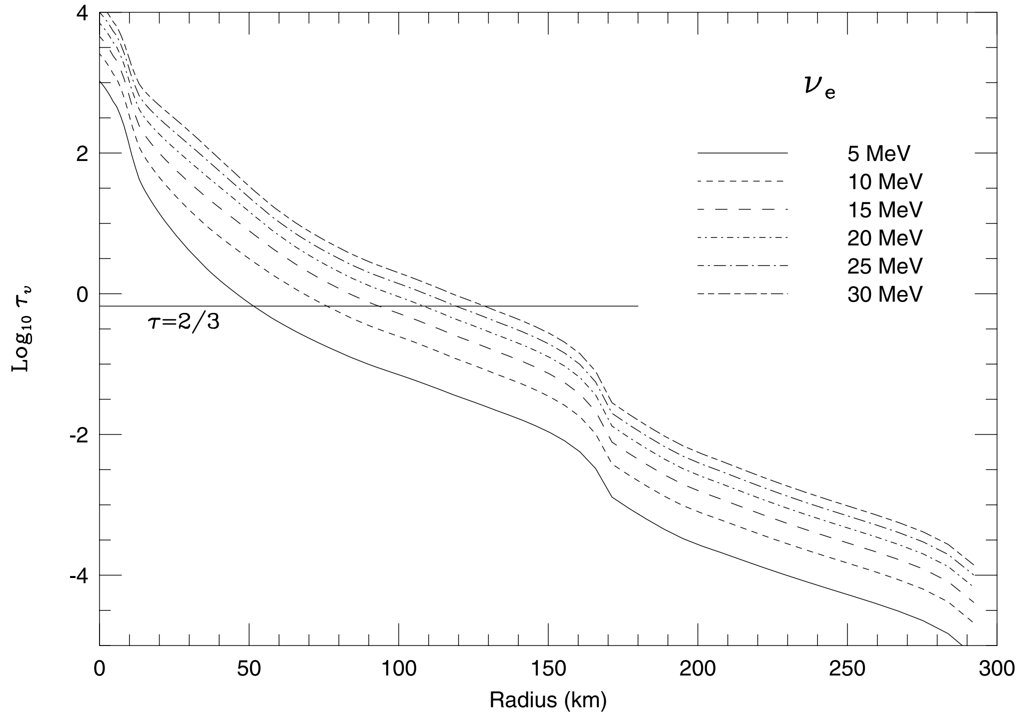

FIG. 2.—ν_e neutrino optical depth (τ_{ν_e}) vs. radius (in kilometers) for model BM, at various particle energies. As the energy of the neutrino increases the degree of transparency decreases. The dip in the optical depth at 170 km is where the shock (and, hence, a density jump) is located. The solid horizontal line shows where $\tau_{\nu_e} = \frac{2}{3}$.

of the shock. This situation has a bearing on the strength of the high-energy spectral tail. Note that for the ν_e and $\bar{\nu}_e$ neutrinos the gain region for model BM, between ~ 110 km and the shock, resides at optical depths below ~ 0.1 near the peak of their respective emergent spectra. For slightly higher neutrino energies, the optical depth of this region is correspondingly higher. Hence, energy deposition in this semitransparent region is problematic and requires a full transport code to study adequately.

It is important to distinguish absorption from scattering. The scattering albedo is the a priori probability that an interaction is a scattering (κ_ν/χ_ν). It is a function of composi-

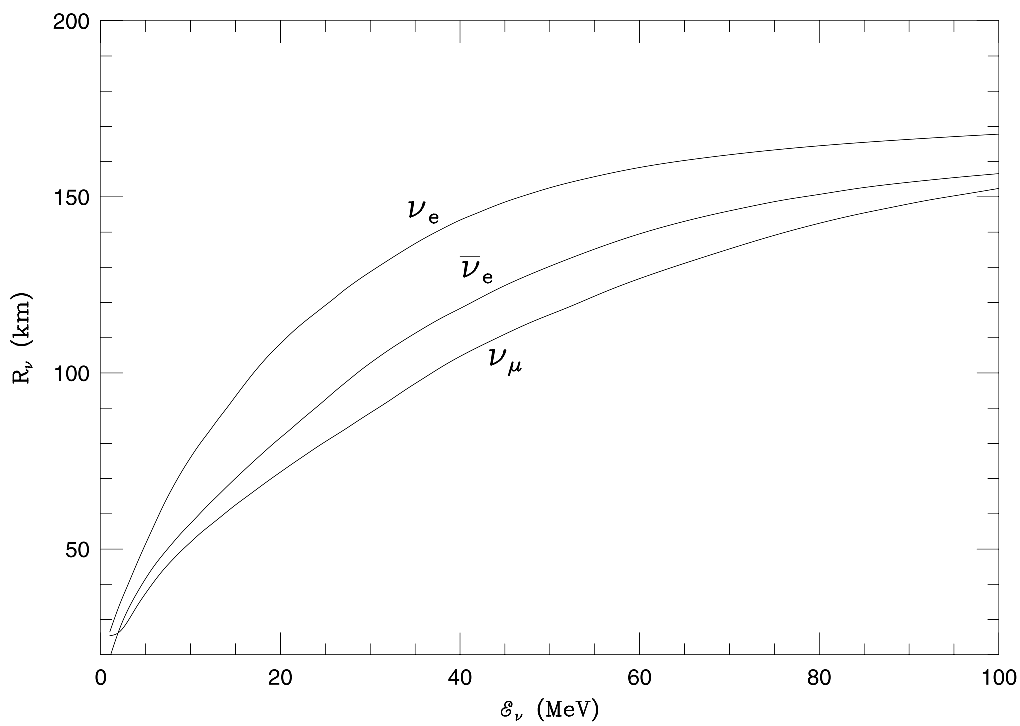

FIG. 3.—Neutrinosphere radii vs. neutrino energy for ν_e, $\bar{\nu}_e$, and "ν_μ" neutrinos. For a given neutrino energy, the ν_μ neutrinos decouple first, resulting in a $\tau = \frac{2}{3}$ radius that is smaller than that for either ν_e or $\bar{\nu}_e$ neutrinos. The hierarchy in decoupling radii of $\nu_e > \bar{\nu}_e > \nu_\mu$ is manifest.

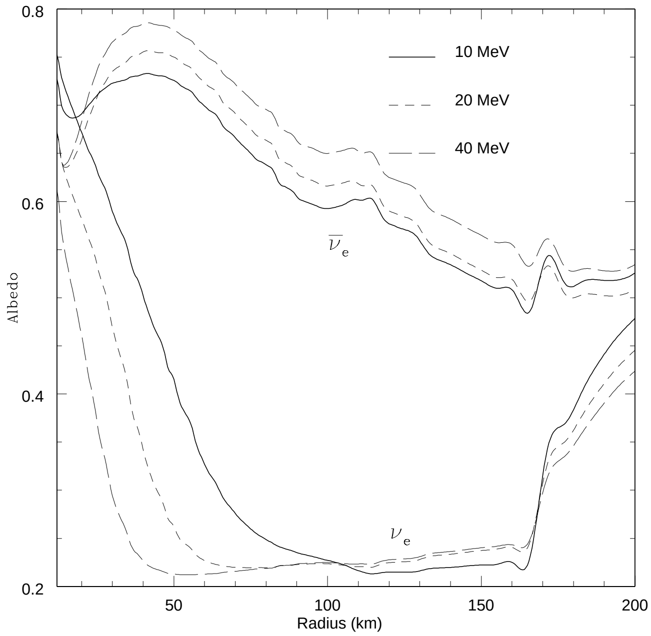

FIG. 4.—ν_e and $\bar{\nu}_e$ scattering albedos vs. radius for neutrino energies of 10, 20, and 40 MeV. The shock is at $\sim$170 km. The increases in the ν_e albedo at small radii can be traced to e^- blocking of ν_e absorption on neutrons, predominantly.

tion, neutrino energy, neutrino type, and final-state blocking. For ν_e neutrinos, the excess of neutrons over protons in the free-nucleon, high-entropy region interior to the shock results in an albedo near 0.25, while for the $\bar{\nu}_e$ neutrinos it is 0.5–0.6. Figure 4 depicts the model BM scattering albedos versus radius as a function of energy for ν_e and $\bar{\nu}_e$ neutrinos. In the interior, the absorption process, $\nu_e + n \rightarrow e^- + p$, is suppressed by blocking due to final-state electrons. This results in an elevated scattering albedo for the lower energy ν_e neutrinos. For ν_μ neutrinos in model BM, scattering predominates and exterior to 20 km the albedo is above 0.95. Such a scattering albedo for the ν_μ neutrinos makes its transport a thermalization depth problem that cannot be easily handled with flux limiters.

8.2. *Emergent Spectra, Luminosities, and Heating Rates*

The emergent neutrino spectra and luminosities are functions of the progenitor, and they evolve. Generally, the spectra after bounce harden with time (Mayle et al. 1987), but after hundreds of milliseconds or as accretion reverses into explosion (or otherwise subsides), the spectra start to soften. The residue then cools inexorably over many seconds, like a clinker plucked from a smelter (Burrows & Lattimer 1986). Our models are merely snapshots, but they serve as contexts in which to study the influence of various effects and physics. In addition, the results can serve as benchmarks against which to compare those from approximate schemes (see § 9). The luminosity profiles and spectra for model BM are depicted in Figures 5 and 6, respectively. The ν_μ neutrino luminosity includes that due to ν_μ, $\bar{\nu}_\mu$, ν_τ, and $\bar{\nu}_\tau$ neutrinos. The steeper rise and plateau of the ν_μ luminosity is a consequence of the small scattering albedo and deeper point of energy decoupling, even though the $\tau = \frac{2}{3}$ surface is at larger radii. The peaks in the ν_e and $\bar{\nu}_e$ luminosities mark the inner radius of the gain region, which resides where the luminosity slope is negative. The rapid variation in ν_e luminosity at smaller radii is a consequence of the variation in the temperature slope in the original model, itself presumably a consequence of sparse zoning.

The asymptotic ν_e and $\bar{\nu}_e$ luminosities are 4.3×10^{51} ergs s^{-1} and 3.1×10^{51} ergs s^{-1}, respectively, 13% higher and 9% lower than the corresponding "BOLTZTRAN" numbers from Messer et al. (1998). The differences must

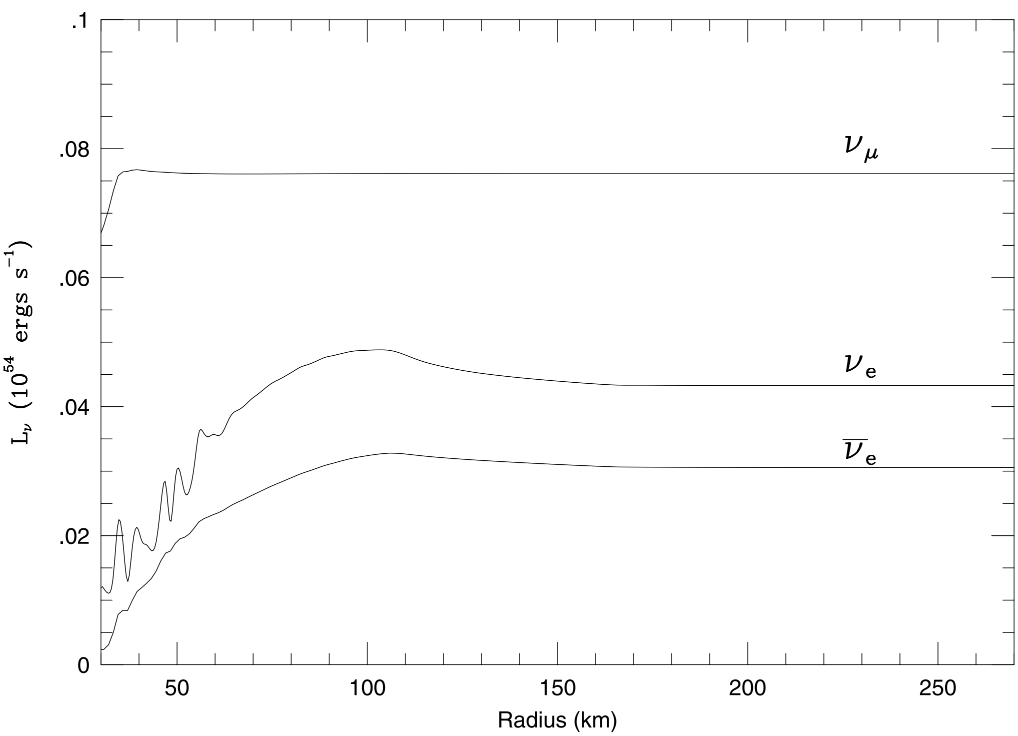

FIG. 5.—Model BM ν_e, $\bar{\nu}_e$, and ν_μ luminosities vs. radius (in kilometers). The "ν_μ" luminosity is the sum of the ν_μ, $\bar{\nu}_\mu$, ν_τ, and $\bar{\nu}_\tau$ neutrino luminosities. The modest peaks mark the inner radius of the gain region, in which, because of net absorption, the luminosity slope is gently negative.

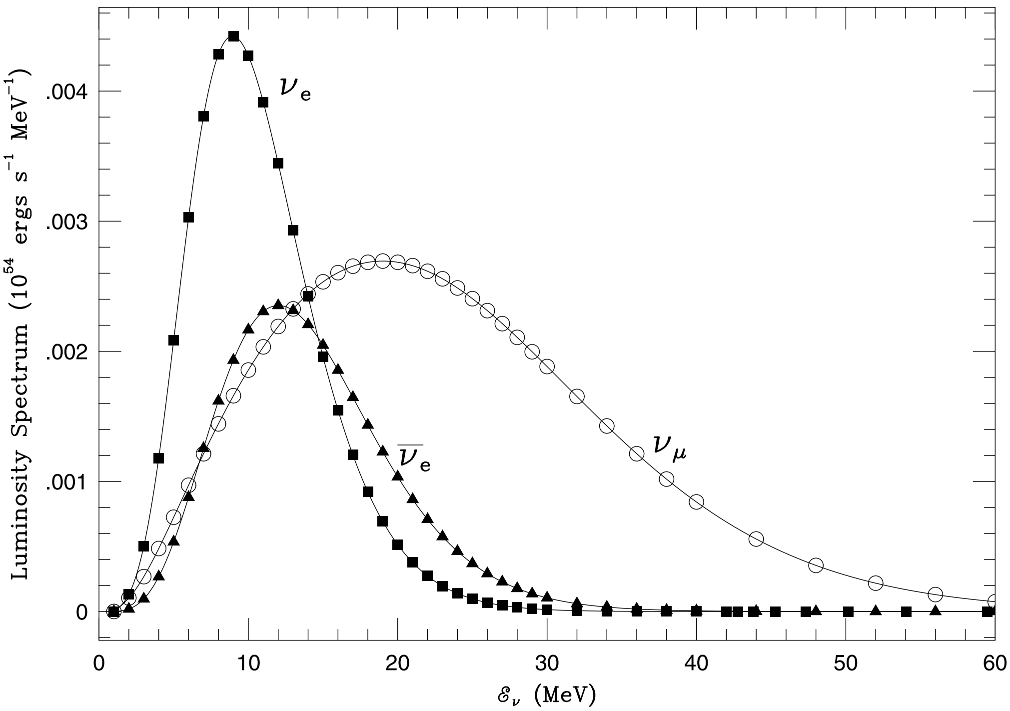

FIG. 6.—Model BM emergent neutrino luminosity spectra for the three neutrino types. The symbols indicate the positions of the energy groups (ν_e: *filled squares*; $\bar{\nu}_e$: *filled triangles*; ν_μ: *open circles*).

stem from a combination of differences in our numerical algorithms, in our spatial, angular, and energy zoning, and in our cross sections. Our emergent spectra for model BM are given in Figure 6. The hardness hierarchy of $\nu_e < \bar{\nu}_e < \nu_\mu$ is manifest, as is the dominance of ν_μ neutrinos at high energies. The ν_e and $\bar{\nu}_e$ spectra can be fit by a Fermi-Dirac distribution with temperatures and η of 2.22 MeV and 3.16 for the ν_e neutrinos and 2.80 MeV and 3.48 for the $\bar{\nu}_e$ neutrinos. The best Fermi-Dirac fit to the ν_μ neutrino spectrum has a negative η, which might as well be $-\infty$. Note that the emergent ν_μ spectrum shown in Figure 6 was calculated with the bremsstrahlung ζ set equal to 0.5. The dependence of the ν_μ spectrum on ζ will be explored in § 10.

The corresponding energy-integrated inverse flux factors ($\int J_\nu d\varepsilon / \int H_\nu d\varepsilon$) for model BM are plotted versus radius in Figure 7. Figure 8 depicts the unintegrated ν_e inverse flux factors (J_ν/H_ν) at given radii versus neutrino energy. Since neutrino-matter heating terms are proportional to J_ν, the higher the inverse flux factor the more efficiently a given energy flux (luminosity) heats the matter in the semitransparent gain region. Different transport algorithms result in different inverse flux factors, so getting this term right can be important to the viability of the neutrino-driven supernova mechanism (Mezzacappa et al. 1998) and to the acceleration and entropy of the postexplosion wind (Burrows 1998a, 1998b). In addition, the harder the spectrum, the stronger the neutrino-matter coupling, so the ν_e and $\bar{\nu}_e$ neutrino spectra versus radius around and exterior to the neutrinospheres have a direct bearing on the heating rate.

Figure 9 portrays the H_ν and J_ν spectra as the ν_e neutrinos decouple. As this figure shows, at large radii H_ν and J_ν are the same, but at depth J_ν is much larger than H_ν. The precise values of J_ν as the neutrinos decouple determine the matter heating rate. The energy-integrated heating and cooling rates versus radius for model BM for all neutrino species individually are given in Figure 10. The positions of radiative equilibrium are indicated with a large dot and the inner radius of the gain region for each neutrino is denoted by an X. Note that the gain region identified on Figure 10 coincides with the gain region determined from the luminosity plot (Fig. 5). Also included on Figure 10 are the heating rates due to $\nu_e - \bar{\nu}_e$ annihilation and to $\nu_\mu - \bar{\nu}_\mu$ and $\nu_\tau - \bar{\nu}_\tau$ annihilation, done properly with the appropriate angular factors (Janka 1991). Aside from being competitive in the irrelevant unshocked regime, heating due to neutrino pair annihilation is meager, at best. In addition, because of the fuzziness of the neutrinospheres, the heating rate per cm^{-3} does not follow the $1/r^8$ law that might have been appropriate for a sharp neutrinosphere. The difference between the heating and cooling curves, the "net gain," for model BM is given by a solid line in Figure 11, to be compared with Figure 8 of Messer et al. (1998). We obtain similar heating rates throughout most of the supernova atmosphere, but slightly greater rates between 110 and 130 km. This slight difference could be due to a combination of things, including different techniques, different cross sections, slightly different equations of state, or our better angular and energy resolution.

8.3. *Consequences of Various Physical Terms*

The neutrino radiation fields depend upon terms that incorporate various physical effects. It is conceptually useful to gauge these terms by their influence on the emergent spectra and on the heating rate. Examples of effects that may or may not be included in simpler schemes are the final-state electron blocking term for the charged-current absorption process (§ 6.1), stimulated absorption corrections (§ 5), weak magnetism and recoil (§ 6.1), and the velocity advection, aberration, and Doppler shift terms in the transport equation (eqs. [2] and [4]). The net gain and the

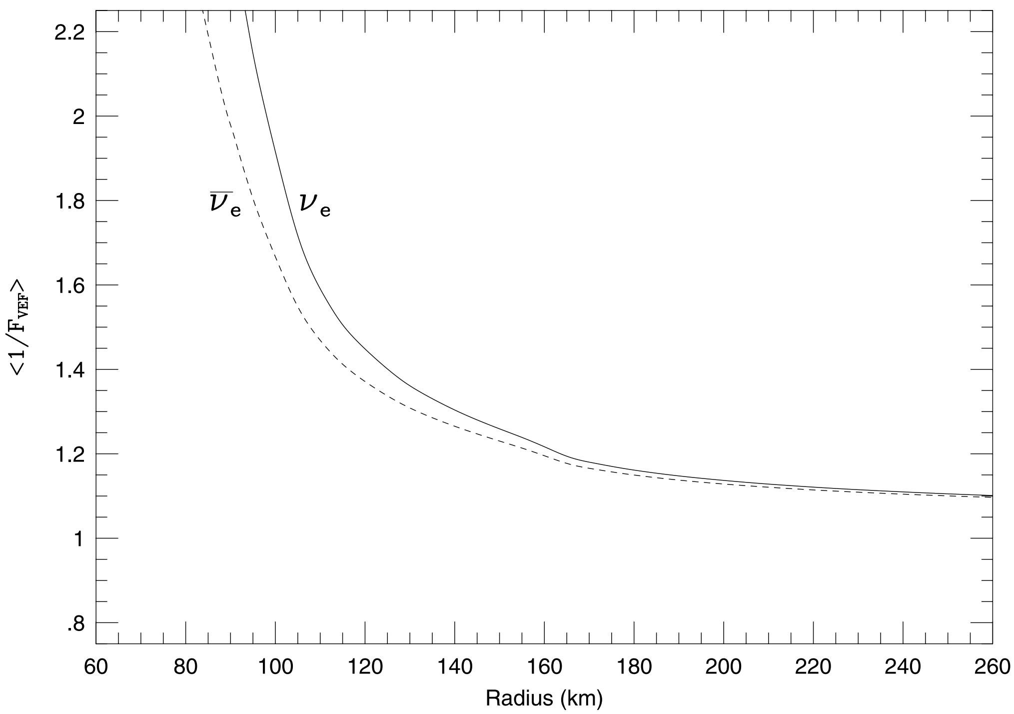

FIG. 7.—Energy-integrated inverse flux factor ($\langle 1/F_\nu \rangle$) as a function of radius for ν_e and $\bar{\nu}_e$ neutrinos. The sharp increase in $\langle 1/F_{\rm VEF} \rangle$ at 110 km occurs just inside the gain radius, where the neutrinos are starting to decouple from the matter. At large radii (*off the plot*), the inverse flux factors approach the unity expected for the free-streaming regime.

ν_e and $\bar{\nu}_e$ neutrino spectra for model BM, with and without the blocking, weak magnetism and recoil, or the stimulated absorption terms, are depicted in Figures 11 and 12. The blocking correction to the emergent ν_e luminosity is $\sim 15\%$, and that due to stimulated absorption is $\sim -3.5\%$. The blocking and stimulated absorption corrections to the emergent $\bar{\nu}_e$ neutrino luminosity are of opposite sign and approximately equal to -6.0% and 3.5%, respectively. Blocking and stimulated absorption shift the emergent ν_e and $\bar{\nu}_e$ spectra in opposite directions in a given energy group by as much as $\sim 20\%$ and $\sim -8\%$, respectively, because of blocking and $\sim -5.5\%$ and $\sim 6.5\%$, respectively, because of stimulated absorption. Blocking increases the net gain by 10%–20%, while stimulated absorption

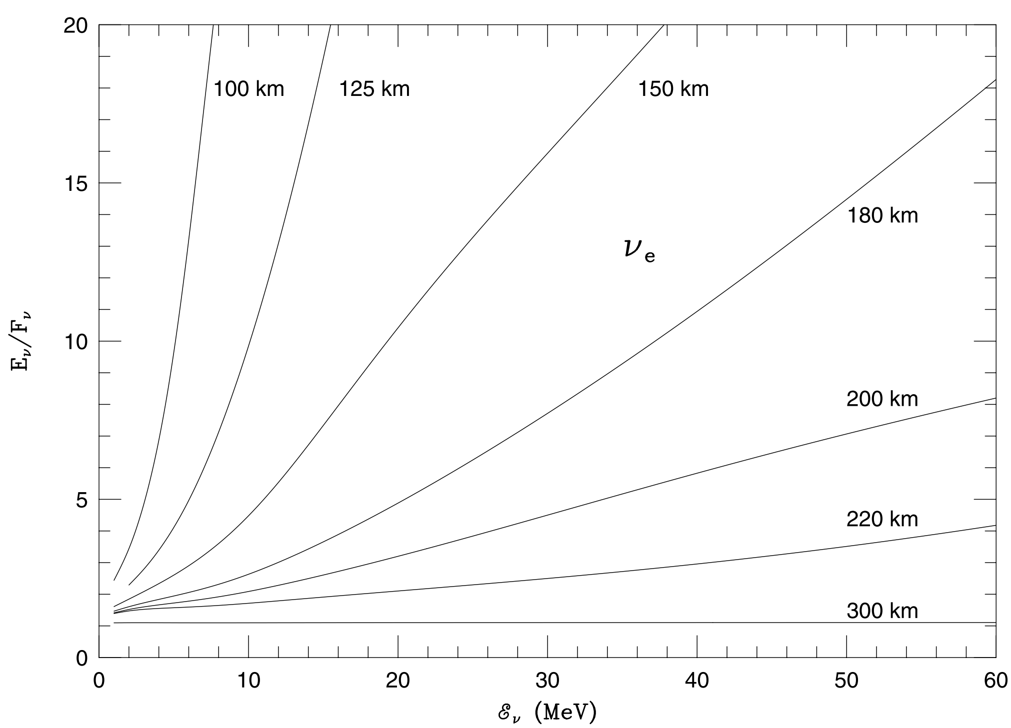

FIG. 8.—Model BM ratios of the ν_e neutrino energy density to the ν_e energy flux for radii of 100, 125, 150, 180, 200, 220, and 300 km

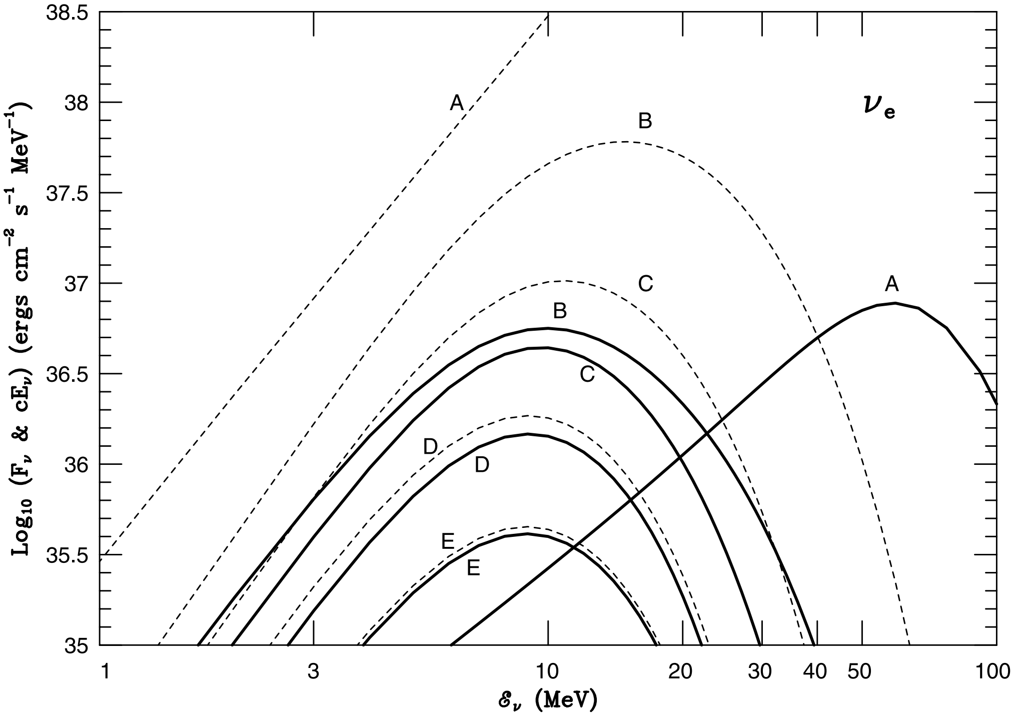

FIG. 9.—ν_e neutrino energy flux (F_ν; *solid line*) and energy density (E_ν; *dashed line*) spectra at various radii. A, B, C, D, and E denote radii at 50, 130, 200, 250, and 300 km. At depth, the spectra are very different, but they converge at large distances from the neutrinospheres. At these large distances, the unintegrated flux factor, F_ν/cE_ν, is unity.

decreases it by less than 5%. Without electron blocking, the absorption cross sections are artificially enhanced. Since the degree of degeneracy is different in the envelope and around the neutrinospheres, the magnitude of this effect in the two regions is different, enhancing the emergent luminosity more than it decreases the coupling in the periphery. Stimulated absorption has the opposite effect (§ 5), but its effect in the core and in the envelope is similarly differential.

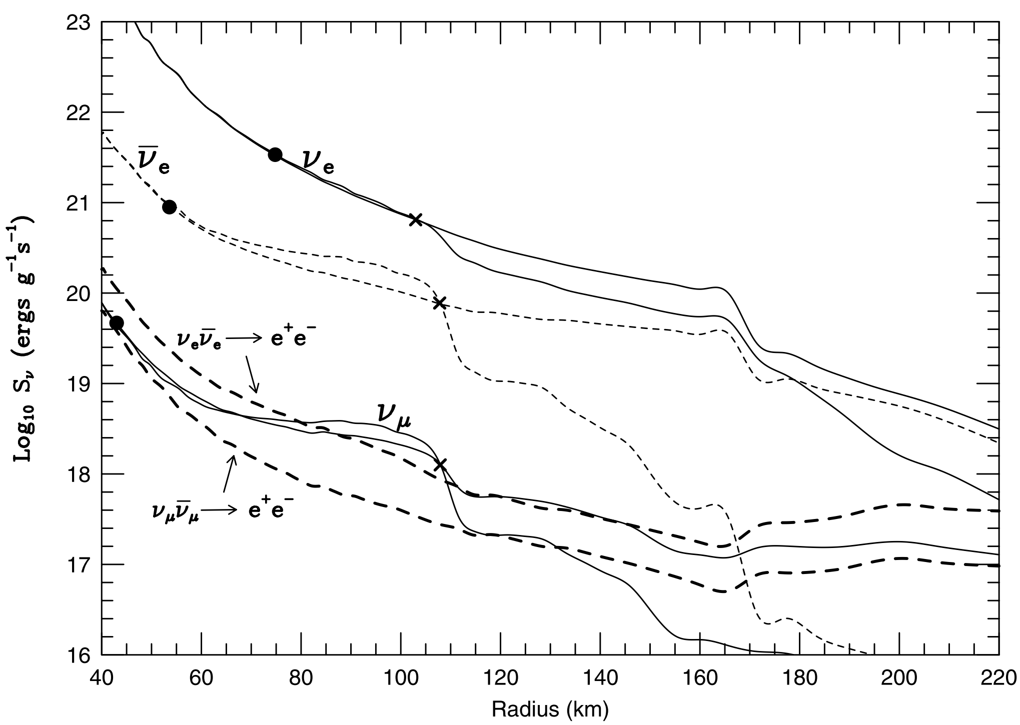

FIG. 10.—Model BM heating and cooling rates (in ergs g^{-1} s^{-1}) vs. radius (in kilometers). The heating and cooling rates for the three neutrino species are shown, along with the $\nu - \bar{\nu}$ annihilation energy deposition rates. The solid points indicate where radiative equilibrium is achieved for each neutrino species. The X indicate the positions of the gain radii for the respective neutrino types. The top two solid lines are the heating and cooling curves for theν_e neutrinos. The dashed lines are the heating and cooling curves for the $\bar{\nu}_e$ neutrinos. The bottom two solid lines are the heating and cooling curves for ν_μ neutrinos. The bold dashed curves are the heating rates for (*top*) the $\nu_e \bar{\nu}_e \rightarrow e^+e^-$ process and (*bottom*) both the $\nu_\mu \bar{\nu}_\mu \rightarrow e^+e^-$ and $\nu_\tau \bar{\nu}_\tau \rightarrow e^+e^-$ processes.

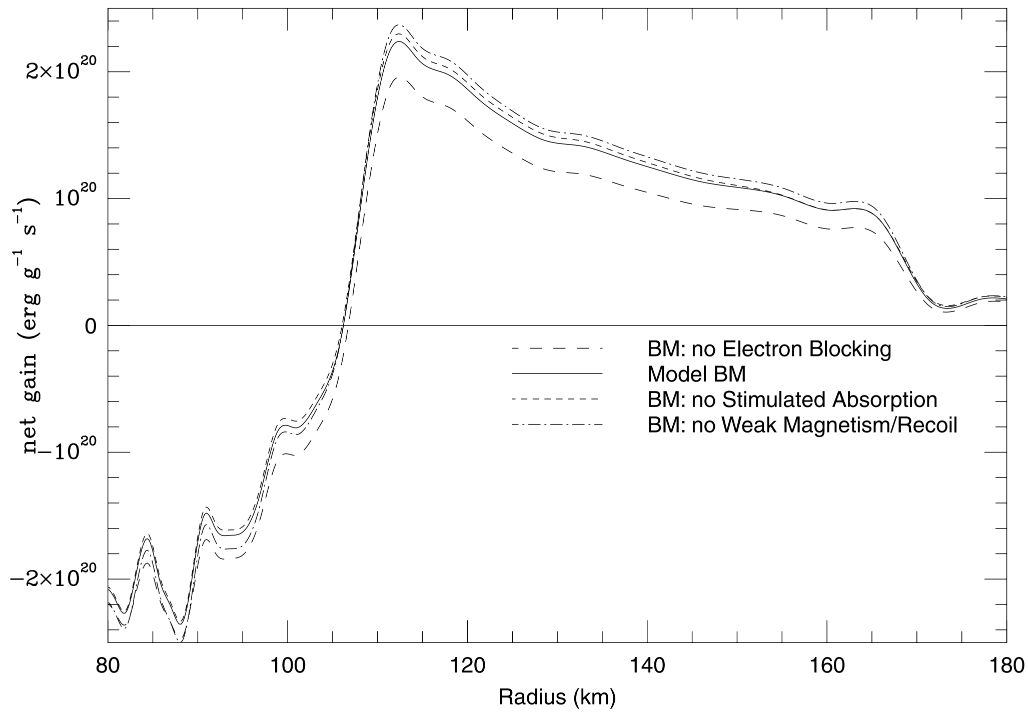

FIG. 11.—Net heating rate (net gain) for various BM models vs. radius. The fiducial model (*solid lines*) is compared to models with no stimulated absorption (*short-dashed line*), with no e^- blocking (*long-dashed line*), or with no weak magnetism/recoil (*dot-dashed line*). The absence of either stimulated absorption or weak magnetism/recoil would result in an increase in neutrino absorption and, thus, a greater heating rate. The absence of e^- blocking would result in a decrease in the net gain.

In these model BM calculations, the effects of weak magnetism and recoil on the emergent ν_e and $\bar{\nu}_e$ neutrino spectra and luminosities are small ($\leq 2.0\%$). This is due in part to the fact that the presence of scattering mutes the effect of changes in the absorption cross section through the thermalization depth effect. Because of the modest scattering albedo (Fig. 4), the response of the radial dependence of the radiation field to changes in the absorption cross section is not linear with the change in the absorption cross section itself. The increase in the net gain that one would anticipate because of any increase in the $\bar{\nu}_e$ luminosity is countered by the concomitant decrease in the absorption cross section in the gain region.

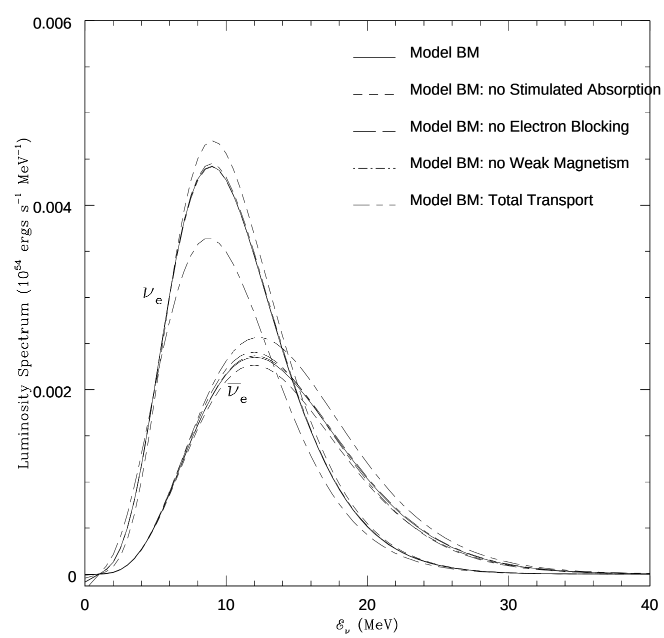

FIG. 12.—Emergent luminosity spectrum for both the ν_e and $\bar{\nu}_e$ neutrinos for our fiducial model BM (*solid line*), compared with models without stimulated absorption (*short-dashed line*), e^- blocking (*long-dashed line*), or weak magnetism/recoil (*dot-dashed line*). Also included is a model for which the total scattering cross section is substituted for the transport cross section (*short-dashed–long-dashed line*).

The winds that emerge from protoneutron stars after their envelopes supernova are powered by neutrino energy deposition in the expanding gas. Just as with the supernova itself, the wind mass and enthalpy fluxes, velocities, entropies, and compositions are influenced by details of neutrino-matter coupling and neutrino transport. The distribution of the heating determines the magnitude, spatial extent, and timescale of acceleration. In turn, the degree of *r*-processing in the ejecta is a function of the expansion timescale, the asymptotic Y_e, and entropy (Woosley & Hoffman 1992; Qian & Woosley 1996). Hence, it is important to gauge the relative strengths of the various terms that determine the degree and distribution of neutrino-matter heating.

The effect of the velocity terms on the emergent ν_e and $\bar{\nu}_e$ spectra for model W is depicted in Figure 13. Model W is the postexplosion wind model from Burrows et al. (1995), in which the velocities at large radii are $\sim$30,000 km s^{-1}. Of course, at small radii they are zero. As Figure 13 shows, the velocity effects collectively boost the emergent spectra of model W in a given energy group by $\sim$15%, with a corresponding boost in the ν_e and $\bar{\nu}_e$ luminosities by 15% and 13%, respectively. This is mostly a consequence of the Doppler shift of the radiation field. Because of the smaller velocities in the important accretion regions in model BM, the velocity corrections for that model are much smaller

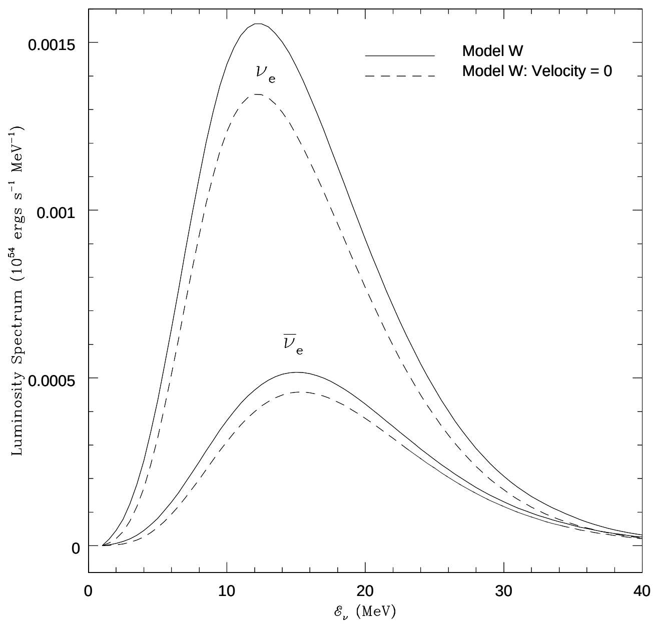

FIG. 13.—Emergent ν_e luminosity spectrum for the wind model W with a velocity field (*solid line*) and without a velocity field (*dashed line*), vs. energy in MeV. The velocity terms boost the spectrum that emerges from a proto–neutron star with a wind by $\sim 15\%$.

($\leq 5\%$). Figure 14 shows the net gain in model W for our fiducial model, as well as without blocking, velocity corrections, or weak magnetism/recoil corrections and implies that various terms not easily or often included in flux-limited or energy-integrated transport can each make a $\sim 10\%$ difference in the parameters of the wind. Note that though the weak magnetism/recoil corrections for model BM are small, those for model W are modest. This result implies that the importance of absorption cross section changes is a function of the specific thermal and composition profiles. What distinguishes the wind is the more abrupt transition from the diffusive to the streaming regime and the lower Y_e value in its decoupling region (Fig. 1). Whereas, in model BM the slight increase in the core luminosity due to the inclusion of the weak magnetism/recoil term is nullified by the decrease in the absorption opacity in the envelope when determining the net gain, in model W the slight increase in the luminosity due to the lower absorption cross section that is a consequence of weak magnetism (particularly for the $\bar{\nu}_e$ neutrinos) is not adequate to counter the resulting greater transparency of the envelope. The Y_e at the base of the wind's atmosphere is smaller than that near the neutrinospheres in model BM, with the result that the scattering albedo for the $\bar{\nu}_e$ neutrinos is larger there. This results in a smaller increase in the emergent luminosity that cannot compensate for the increase in the transparency of the wind's mantle.

The anisotropy of neutrino-nucleon scattering and the difference between the transport and the total cross sections (eq. [17]) can in principle translate into larger inverse flux factors and, hence, greater net gain. Backscattering increases J_ν for a given H_ν and delays the transition from isotropic to forward-peaked radiation fields. However, since absorption plays an important role for the ν_e and $\bar{\nu}_e$ neutrinos and their scattering albedos are not very close to one, the backscatter effect is muted. The upshot is that anisotropy accounts for only $\sim 2\%$ of the net gain and results in shifts of less than 1% in the ν_e or $\bar{\nu}_e$ spectra.

9. FLUX LIMITERS

It is common to seek methods for solving equations (12) and (13) without employing the full machinery of transport.

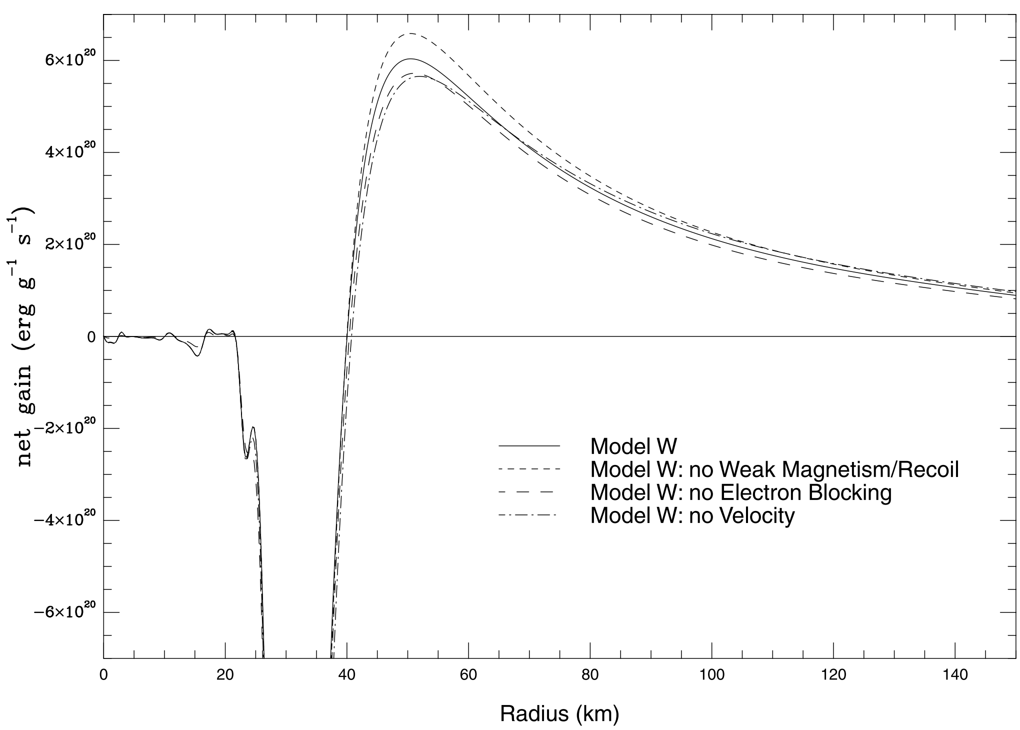

FIG. 14.—Net heating rate (net gain) vs. radius (in kilometers) for wind model W. The fiducial model (*solid line*) is compared with models for which either weak magnetism/recoil (*short-dashed line*) or e^- blocking (*long-dashed line*) is ignored. Also included is a model for which the velocities were set equal to zero (*dot-dashed line*).

In principle, such methods simplify the mathematics and speed solution, but they compromise accuracy. Equations (12) and (13) are the first two equations in a moment hierarchy in which each moment equation involves still higher order moments; to solve such a hierarchy precisely requires the solution of an infinite number of moment equations. The simplifying ansatz often introduced is that higher order moments can be written in terms of lower order moments, thereby closing the system of equations. However, these so-called closure relations can vary a great deal. The most common closure is the flux limiter.

In flux-limited schemes, equation (13) is reduced to its diffusion form in which H_ν is set equal to the product of the gradient of P_ν and a coefficient (the flux limiter), P_ν is set equal to $\frac{1}{3}J_\nu$ (the Eddington closure), and this expression for H_ν is inserted into the divergence term in equation (12). Only this zeroth-moment (energy) equation is solved. The third-order moment, N_ν, important for multienergy group calculations in moving media, is generally ignored. The art of this approach is in the choice of the flux limiter, so called because the coefficient is constructed in such a way that the flux, otherwise mathematically diffusive in this scheme, does not exceed the streaming limit, J_ν. This is necessitated by the dropping of equation (13), with its causality-enforcing time derivative. All angular information is lost, though some flux limiters are derived under certain assumptions about the angular distribution (cf. Levermore & Pomraning 1981). Examples of flux limiters that have been employed in supernova calculations are the Wilson (Bowers & Wilson 1982) and Bruenn (1985; Messer et al. 1998). Their prescription for the flux is

$$H_\nu = -\frac{\lambda_\nu}{3}\left(1 + \frac{|R|}{3}\,\Xi_F\right)^{-1}\frac{\partial J_\nu}{\partial r}\,, \tag{52}$$

where $\Xi_F = 1 + 3/(1 + |R|/2 + R^2/8)$ for Wilson and $\Xi_F = 1.0$ for Bruenn, $R = -\lambda_\nu\,\partial \ln J_\nu/\partial r$, and λ_ν is the transport mean free path. The expression in parentheses is the limiter. Hence, in flux-limiter closures, H_ν is a function of only J_ν and its derivative (or J_ν and R) and p_ν $(=P_\nu/J_\nu)$ is set equal to $\frac{1}{3}$. Note that the Knudsen parameter (R) is small in the diffusion limit. The subscript ν is a reminder that these equations apply for each energy group. It is important to note what should be obvious: not all flux limiters are the same, nor are their quantitative consequences. Hence, there is not a uniform "flux limiter" result. For instance, the multigroup flux-limited diffusion (MGFLD) scheme of Messer et al. (1998) is merely one such approach. The results of employing a given flux limiter can deviate from the correct result as much as can the results derived using various flux limiters deviate from one another.

9.1. *Angular Distributions*

To gauge the character of the proper angular dependence of the neutrino distribution functions in the supernova context, we provide in Figure 15 the model BM Eddington factor (p_ν) versus radius for ν_e neutrinos, at particle energies from 5 to 30 MeV. As we would expect from the decoupling hierarchy, the ν_μ Eddington factors start their rise from the isotropic value of $\frac{1}{3}$ from the deepest layers. However, for all neutrino species, particularly for the $\bar{\nu}_e$ and ν_μ neutrinos, the Eddington factor is a stiff function of energy and only gradually makes the transition from $\frac{1}{3}$ to 0.75 over a region that can be 50 to 150 km wide. Many flux limiters effect the

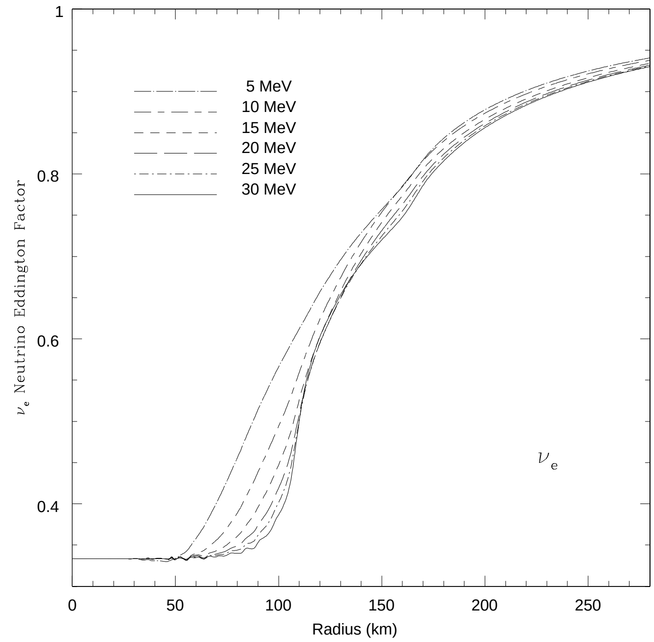

FIG. 15.—Eddington factor for ν_e neutrinos vs. radius (in kilometers) at various ν_e neutrino energies. At depth, in the diffusive region the Eddington factors converge to $\frac{1}{3}$. At large radii, the Eddington factors approach unity. The low-energy neutrinos are the first to decouple, and their Eddington factors approach unity faster than those of the higher energy neutrinos.

related transition from diffusion to free streaming early (at higher τ_ν) and within an unphysically narrow range in radius and τ_ν. This can be seen in Figure 16, where the Bruenn and Wilson flux limiters for ν_e neutrinos at 20 MeV in model BM are compared with the "effective" flux limiter derived using full transport. Approximately 20 km interior to the appropriate point, the Bruenn and Wilson limiters begin to deviate from the diffusion value of 1.0.

Polar plots depicting representative angular distributions of the model BM $\bar{\nu}_e$ specific intensity (I_ν) field for an energy of 15 MeV are presented as solid lines in Figure 17. The transition from isotropy to forward-peaked is clear, as is the gradual nature of that transition. There is no corresponding angular function for either the Bruenn or Wilson limiter.

Complementary to this polar plot are Figures 18, 19, and 20 of the full transport phase-space densities ($\mathscr{F}_\nu$) versus energy at various radii and for all the neutrino species. Depicted are the phase-space densities along the 0° and 90° directions. For the ν_e neutrinos, the degree of degeneracy at depth is clear; one can almost read the ν_e chemical potentials off the graph. From Figure 19, we see that the occupancy of the $\bar{\nu}_e$ neutrino states is generically low, but from Figure 20 we see that at depth and for low energies the occupancy of the ν_μ neutrino states can approach 0.5. Blocking due to final-state ν_μ occupancy is generally unimportant in the pair source terms, since the peak energies of the pair source functions are always significantly above the energies at which $\mathscr{F}_\nu$ is high.

Among other things, Figures 18, 19, and 20 convey a sense of the angular dependence of $\mathscr{F}_\nu$, ignored in the standard flux-limiter schemes. At depth, since the radiation fields are isotropic, the 0° and 90° curves are the same. However, with increasing radius and at lower energies, deviations from isotropy manifest themselves; transverse beams are less occupied than forward beams. As expected, at low

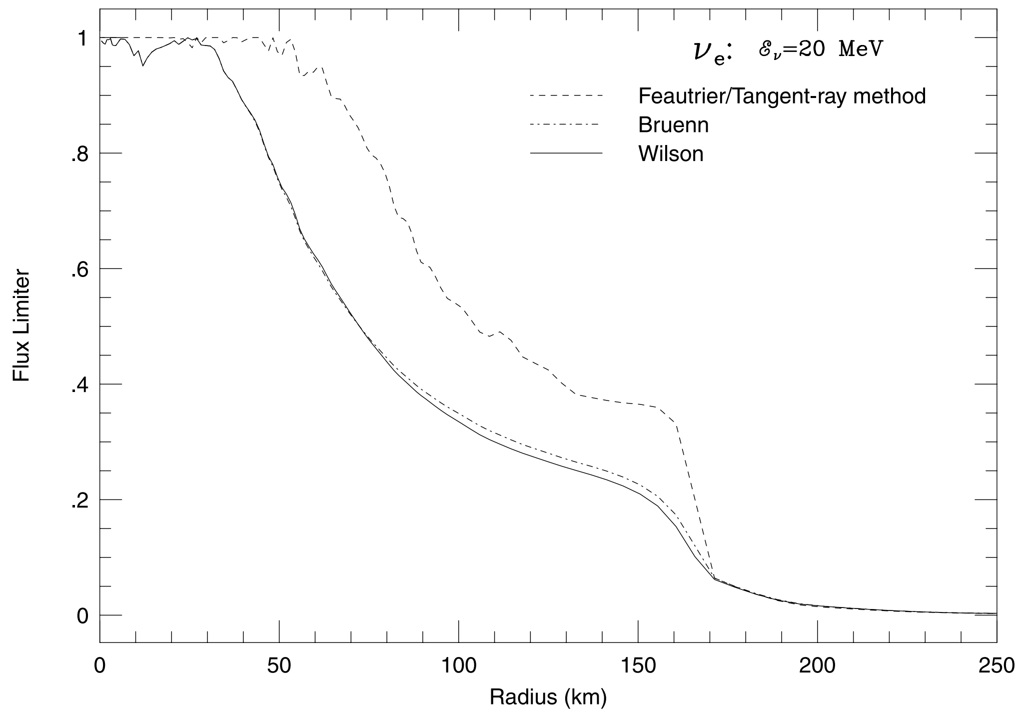

FIG. 16.—Electron neutrino flux limiter profiles vs. radius (in kilometers) for model BM using Bruenn's flux limiter (*dot-dashed line*), Wilson's flux limiter (*solid line*), and an artificial flux limiter derived from the full formalism (*dashed line*). The ν_e neutrino energy is 20 MeV. See text and eq. (52) for details.

optical depths this differential effect is quite pronounced. Flux-limited transport schemes are not capable of addressing or illuminating this phenomenology.

9.2. *Neutrino Heating and Emergent Spectra Using Flux Limiters*

Given the nuances in the angular distributions of the neutrino radiation fields portrayed in Figures 15–20, it is no wonder that flux limiters only inadequately represent the radiation energy density profiles, emergent spectra, and net gain in the semitransparent decoupling region. This is made manifest by comparing the emergent spectra and net gain derived using such flux limiters with those same quantities obtained using full transport. Figure 21 compares the emergent ν_e spectrum for the BM model using the full Feautrier/tangent-ray formalism, Bruenn's limiter, and Wilson's

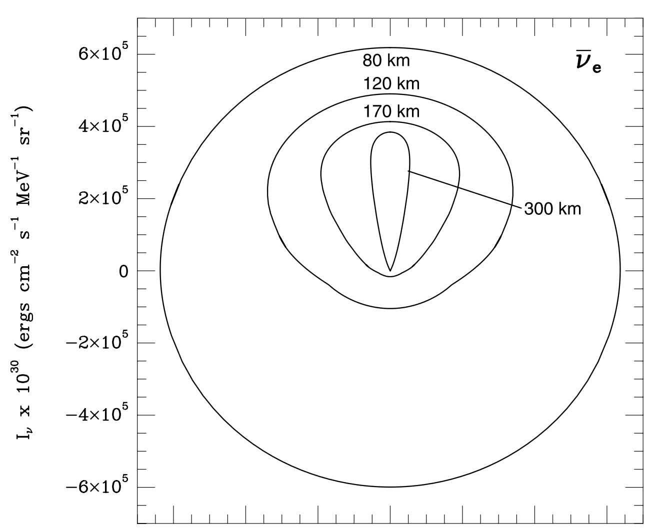

FIG. 17.—Polar plots of the specific intensity (I_ν) of $\bar{\nu}_e$ neutrinos with an energy of 15 MeV. Shown are angular distributions at radii of 80, 120, 170, and 300 km. In the interior, the radiation fields are isotropic and strong. At large radii, the distribution becomes more forward peaked and geometric dilution decreases I_ν. The numbers on the left axis provide the scale, with the negative numbers emphasizing the fact that the rays are pointing backward in this hemisphere.

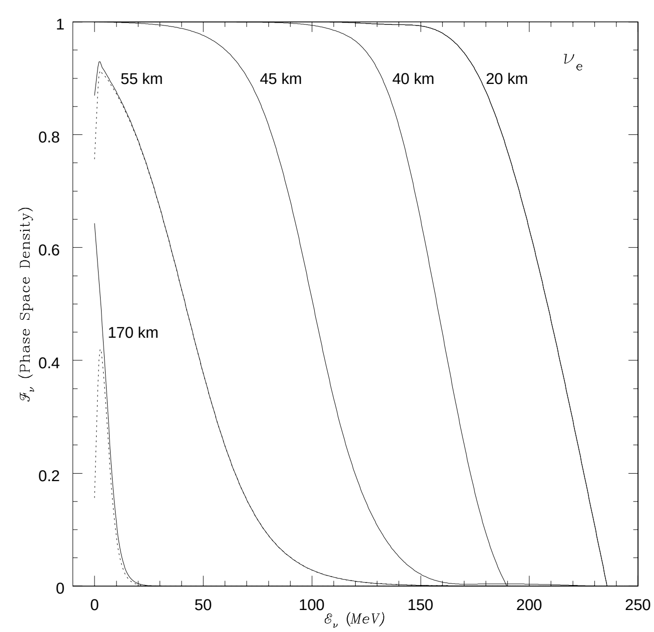

FIG. 18.—Phase-space density ($\mathcal{F}_\nu$) for the ν_e neutrinos vs. neutrino energy in MeV, for various radii from 20 km to 170 km. The solid lines are for the forward direction and the dashed lines are for the transverse direction (at $\sim 90°$ to the radial direction). At small radii, the ν_e neutrinos are degenerate, but at larger radii, and generally at larger energies, they quickly become nondegenerate. Note that at small energies, "larger" radii, and large angles, the degeneracy of the ν_e neutrinos diminishes.

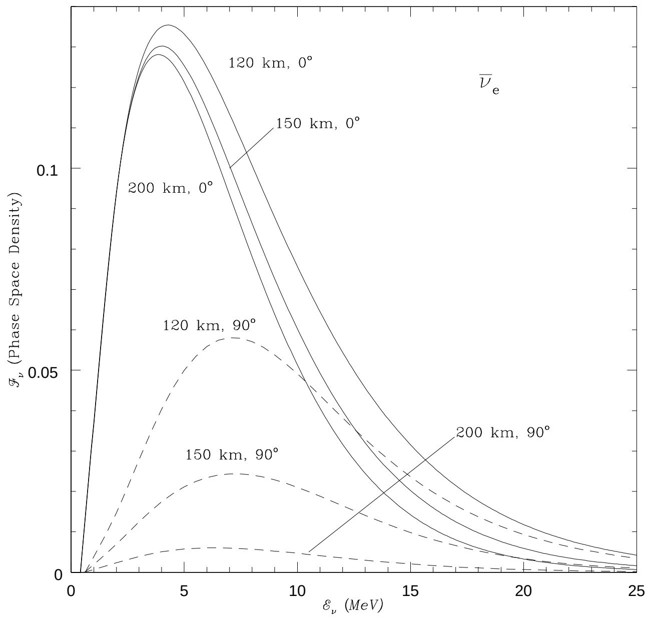

FIG. 19.—Phase-space density ($\mathscr{F}_\nu$) for the $\bar{\nu}_e$ neutrinos vs. neutrino energy in MeV, at radii of 120, 150, and 200 km. The solid lines are for the forward direction and the dashed lines are for the transverse direction (at $\sim 90°$).

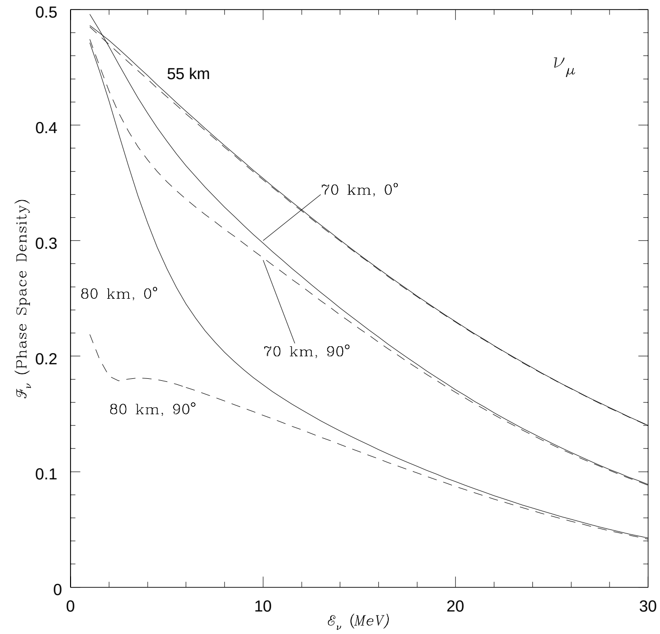

FIG. 20.—Phase-space density ($\mathscr{F}_\nu$) for the ν_μ neutrinos vs. neutrino energy in MeV, at radii of 55, 70, and 80 km. The solid lines are for the forward direction and the dashed lines are for the transverse direction (at $\sim 90°$). At depth, and at lower energies, ν_μ neutrino degeneracy ($\mathscr{F}_\nu$) approaches 0.5, as expected for the situation with no net ν_μ lepton number and, hence, zero chemical potential.

limiter. Though comparisons for many snapshot profiles would be useful, we can still conclude for such an early protoneutron star epoch that Bruenn's limiter, as simple as it is, results in a spectrum that deviates from the more precise spectrum by $\sim 5\%$–10%, while Wilson's limiter, despite its modestly greater complexity, can be off by as much as $\sim 20\%$–30%. Figure 22, in which curves of the net gain (heating) versus radius are compared, tells a similar story: Bruenn's limiter yields net gains that are generally off, but by no more than $\sim 20\%$, while Wilson's can be off by as much as $\sim 50\%$. Figures 21 and 22 serve to illustrate both that all flux limiters are not the same and, in particular, that they can underestimate the net gain in the outer gain region by many tens of percent.

In sum, flux-limiter schemes can miscalculate net heating rates, radiation energy densities (quantities that factor into

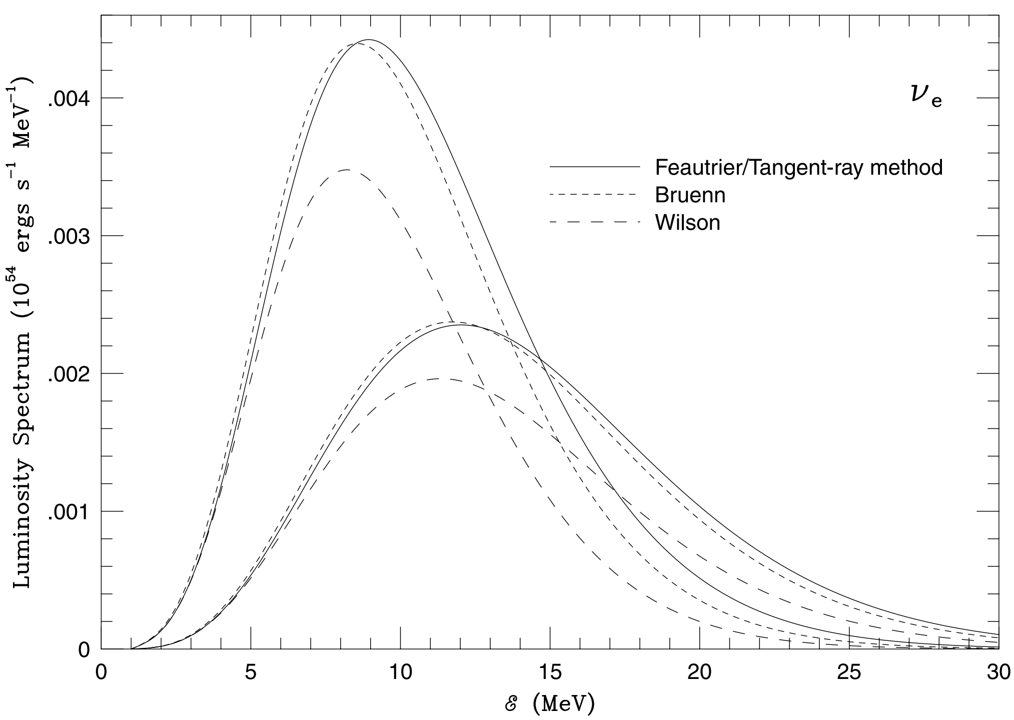

FIG. 21.—Emergent ν_e neutrino luminosity spectrum for model BM using the full Feautrier/tangent-ray formalism (*solid lines*), Bruenn's limiter (*short-dashed lines*), and Wilson's limiter (*long-dashed lines*) (cf. Fig. 6).

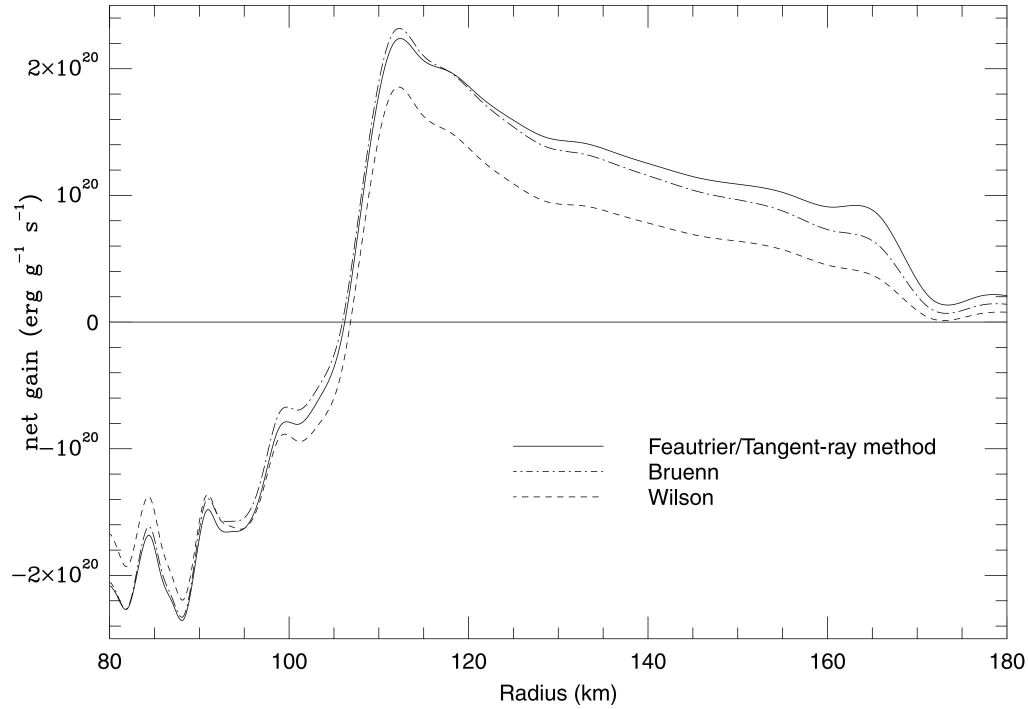

FIG. 22.—Comparison of the net gain (in ergs g^{-1} s^{-1}) vs. radius (in kilometers) for model profile BM, calculated using the full transport formalism of this paper (*solid line*), Bruenn's flux limiter (*dot-dashed line*), and Wilson's flux limiter (*dashed line*) (cf. Fig. 11).

the net gain), emergent spectra, and the inverse flux factors by from 5% to 50% and can artificially accelerate the transition from isotropy to free streaming in the $\tau < 1$ region. This is particularly true for neutrinos, with their extended neutrinospheres. Furthermore, the thermalization depth effect is difficult to handle with flux limiters when the scattering albedo is large. The albedo for ν_μ neutrinos is above 0.90 throughout most of the object. As a result, only full transport can properly handle the enhancement in the effective absorption path because of the frustrated escape caused by scattering.

10. DETERMINANTS OF THE EMERGENT ν_μ NEUTRINO SPECTRUM

The ν_μ and ν_τ neutrinos and their antiparticles carry away from the proto–neutron star more than 50% of its total binding energy. Since they do not participate in charged-current interactions, they energetically decouple at smaller radii and, hence, at larger temperatures, than the other neutrino species. This results in a harder spectrum (Fig. 6) and the hardness hierarchy alluded to in § 8.2. The fact that there are four species is primarily responsible for their major cooling role. Neutrino-matter energy coupling is affected by the inverse production processes of pair annihilation and nucleon-nucleon bremsstrahlung (§ 7), as well as by neutrino-nucleon and neutrino-electron scattering. The proper treatment of energy redistribution by scattering is deferred to a later publication. However, it is clear that scattering generically softens the ν_μ spectra.

Ignoring the potential effects of neutrino oscillations, the emergent ν_μ spectra have a direct bearing on the process of neutrino nucleosynthesis (Woosley et al. 1990) and on the suitability of various underground detectors that rely on neutral-current spallation processes with high energy thresholds. In both cases, the relevant neutral-current interaction cross sections are stiffly increasing functions of neutrino energy, with thresholds above $\sim$15 MeV (Haxton 1990). Hence, they are most sensitive to the ν_μ component and its precise spectrum. In the past, people had thought that the ν_μ spectra were hard, with effective Fermi-Dirac temperatures of $\sim$8–9 MeV and average energies of $\sim$25–30 MeV. However, the ν_μ energy spectrum on Figure 6 can be very approximately fit with a temperature of 7 MeV.

Bremsstrahlung has a major effect on the ν_μ radiation field. The factor ζ in § 7 incorporates a correction for our approximations to the propagator terms and to the nuclear matrix element. In Figure 6, ζ was set equal to 0.5. Using Hannestadt & Raffelt (1998) and our own estimates of the correct propagator terms, we derive that above 10^{13} g cm^{-3} ζ is above 0.7 and that at and around 10^{11} g cm^{-3} ζ is near 0.2. This translates into an "average" ζ of $\sim$0.5 for proto–neutron stars. Figure 23 depicts the consequences of varying ζ from 0.0 to 1.0 in steps of 0.2 for the emergent ν_μ energy spectrum. Because of the presence of an absorption term for every emission term (Kirchhoff's Law; eq. [36]), the strength of the spectrum is not strictly linear in ζ. As Figure 23 demonstrates, nucleon-nucleon bremsstrahlung is softer than e^+e^- annihilation (the other major $\nu_\mu \bar{\nu}_\mu$ source) and can dominate at low energies. Though the emergent spectra are softer, because of the extra source the spectra are also brighter at every energy. Hence, the inclusion of nucleon-nucleon bremsstrahlung increases the flux, while decreasing the average and peak neutrino energies. This is important. At 10 MeV, the ν_μ spectrum can be more than a factor of 2 stronger with bremsstrahlung than without. For energies above $\sim$35 MeV, e^+e^- annihilation still dominates the emergent spectrum. In Figure 23, the lowest curve corresponds to a pure e^+e^- annihilation source. Note that it is demonstrably harder than when ζ is large and that it

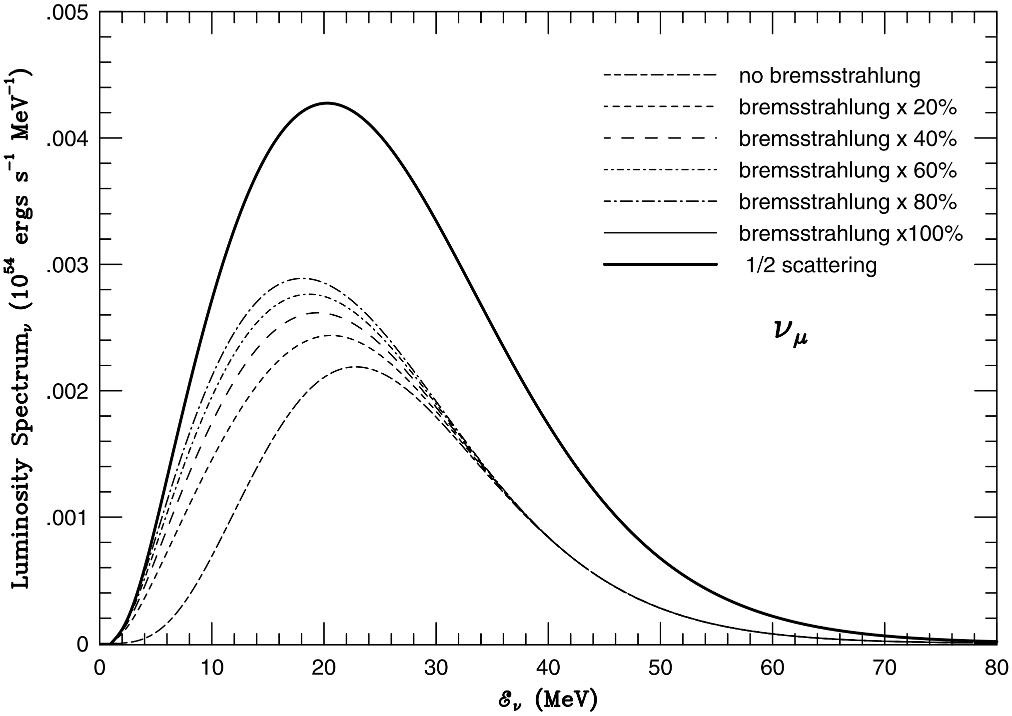

FIG. 23.—Emergent ν_μ luminosity spectra for model BM for bremsstrahlung factors, ζ, of 0.0, 0.2, 0.4, 0.6, 0.8, and 1.0. Also included is the ν_μ spectrum with the ν_μ-nucleon scattering cross section artificially decreased by 50%.

alone is "pinched." Though it still remains to be determined whether nucleon-nucleon bremsstrahlung in supernovae is in fact dominant for ν_μ spectrum formation, Figure 23 suggests that it is, particularly at lower neutrino energies. Since energy transfer due to neutrino-matter scattering and gravitational redshifts will only further soften the emergent spectra, we conclude that ν_μ spectra are indeed softer than traditionally quoted.

Also shown on Figure 23 is an emergent ν_μ spectrum with the scattering cross sections very artificially cut by one half. This curve demonstrates the severe dependence of the spectra on the basic numbers associated with the neutrino-matter interaction. It suggests that if we did not have a fairly good handle on the basic interactions of neutrinos with nucleons our predictions would be quite different and perhaps would be quite wrong.

11. SUMMARY

We have constructed and described an implicit, multigroup, multiangle, multispecies neutrino transfer code to be used in the context of core-collapse supernovae and proto–neutron stars. The basic algorithm embodies the Feautrier and tangent-ray approaches to spherical atmospheres and is conceptually equivalent to various Boltzmann solvers. It is capable of resolving angular distributions and of calculating angular moments to great precision and employs accelerated Λ iteration to achieve rapid convergence. Focusing on neutrino atmospheres, we presented the energy spectra, neutrino heating rates, Eddington factors, angular distributions, and phase space densities for typical postbounce structures. The influence on these quantities, in particular on the net gain, of various corrections to the charged-current cross section and terms in the transport equation were examined and the character of the neutrino radiation fields and spectra was scrutinized. One goal has been to provide a detailed snapshot of the neutrino radial, angular, energy, and species distributions in a typical postbounce environment, including in the protoneutron star context, and to explore the factors that determine the heating rates in the semitransparent gain region, so central to the viability of the neutrino-driven mechanism of supernova explosions. To this end, we focused on the decoupling transition of the emergent neutrinos. Moreover, we compared the emergent spectra and neutrino heating rates obtained using representative flux limiters with those obtained using our Feautrier transport algorithm to gauge the accuracy of those oft-used approximate schemes. Finally, we derived the rate of nucleon-nucleon bremsstrahlung and its neutrino source spectrum and showed for the first time that it probably dominates ν_μ neutrino production and spectrum formation.

The tool that we have developed is meant to explore supernova explosions, protoneutron star cooling, the neutrino signature of core-collapse, neutrino shock breakout, and postexplosion winds, among other things. It is also easily converted into a photon transport code for the study of classical supernova light curves. However, we have yet to generalize the scheme for use in multidimensional supernova simulations or in the general relativistic context, nor have we parallelized it for use on shared-memory machines. Hence, much technical work remains.

Supernova theory has been evolving for 30 years, and in that time our understanding of the neutrino and its interactions has changed substantially. There are now indications from atmospheric and solar neutrino experiments that lepton number is not strictly conserved and that neutrinos may mix. Heating in the proto–neutron star mantle is a subtle sum of competing effects. We have investigated in this paper but a few of these. This effort to fully characterize the neutrino radiation fields is part of a larger effort, as yet unfinished, to understand the mechanism of supernova explosions and their systematics. However, when this puzzle box is eventually opened, precise neutrino transport will certainly be one of the keys.

We are pleased to acknowledge Ray Sawyer, Georg Raffelt, Dimitri Mihalas, Tony Mezzacappa, Chuck Horowitz, John Hayes, and Steve Bruenn for useful contributions and guidance. In addition, we extend special thanks to Jorge Horvath for his help with the bremsstrahlung calculations and to Steve Bruenn and Tony Mezzacappa for providing some of their output in electronic form. This work was supported by the NSF under grant AST 96-17494 and was performed under the auspices of the US Department of Energy by Lawrence Livermore National Laboratory under contract W-7405-Eng-48.

REFERENCES

Aufderheide, M., Fushiki, I., Fuller, G., & Weaver, T. 1994, ApJ, 424, 257
Bethe, H., & Wilson, J. R. 1985, ApJ, 295, 14
Bludman, S. A., & Schinder, P. J. 1988, ApJ, 326, 265
Bowers, R. L., & Wilson, J. R. 1982, ApJS, 50, 15
Brinkmann, R., & Turner, M. S. 1988, Phys. Rev. D, 38, 2340
Bruenn, S. W. 1985, ApJS, 58, 771
Burrows, A. 1998a, in Proc. 9th Workshop on Nuclear Astrophysics, ed. E. Müller & W. Hillebrandt (Garching: Max-Planck-Institut), 76
———. 1998b, in Proc. 18th Texas Symposium on Relativistic Astrophysics, ed. A. Olinto, J. Frieman, & D. Schramm (Singapore: World Scientific), 709
———. 2000, in SN1987A: Ten Years Later, ed. M. M. Phillips & N. B. Suntzeff, in press
Burrows, A., Hayes, J., & Fryxell, B. A. 1995, ApJ, 450, 830
Burrows, A., & Lattimer, J. M. 1986, ApJ, 307, 178
Burrows, A., Mazurek, T. J., & Lattimer, J. M. 1980, ApJ, 251, 325
Burrows, A., & Sawyer, R. F. 1998, Phys. Rev. C, 58, 554
———. 1999, Phys. Rev. C, 59, 510
Cannon, C. J. 1973a, J. Quant. Spectrosc. Radiat. Transfer, 13, 627
———. 1973b, ApJ, 185, 621
Colella, P., & Woodward, P. 1984, J. Comput. Phys., 54, 174
Colgate, S. A., & White, R. H. 1966, ApJ, 143, 626
Dicus, D. A. 1972, Phys. Rev. D, 6, 941
Eastman, R., & Pinto, P. 1993, ApJ, 412, 731
Flowers, E., Sutherland, P., & Bond, J. R. 1975, Phys. Rev. D, 12, 316
Freedman, D. Z. 1974, Phys. Rev. D, 9, 1389
Fryxell, B. A., Müller, E., & Arnett, D. 1991, ApJ, 367, 619
Fuller, G. 1982, ApJ, 252, 741
Fuller, G., Fowler, W. A., & Newman, M. 1980, ApJS, 42, 447
Fuller, G. M., Mayle, R., Meyer, B. S., & Wilson, J. R. 1992, ApJ, 389, 517
Hannestad, S., & Raffelt, G. 1998, ApJ, 507, 339
Haxton, W. 1990, Phys. Rev. Lett., 60, 1999
Herant, M., Benz, W., Hix, R. J., Fryer, C., & Colgate, S. A. 1994, ApJ, 435, 339
Horowitz, C. J. 1997, Phys. Rev. D, 55, 4577
Janka, H.-T. 1991, A&A, 244, 378
Janka, H.-T., Keil, W., Raffelt, G., & Seckel, D. 1996, Phys. Rev. Lett., 76, 2621
Janka, H.-T., & Müller, E. 1994, A&A, 290, 496
Kosirev, N. A. 1934, MNRAS, 94, 430
Larson, E. W. Morel, J. E., & Miller, W. F., Jr. 1987, J. Comput. Phys., 69, 283
Leinson, L. B., Oraevsky, V. N., & Semikoz, V. B. 1988, Phys. Lett. B, 209, 80
Levermore, C. D., & Pomraning, G. C. 1981, ApJ, 248, 321
Lichtenstadt, I., Ron, A., Sack, N., Wagschal, J. J., & Bludman, S. A. 1978, ApJ, 226, 222
Mayle, R., Wilson, J. R., & Schramm, D. N. 1987, ApJ, 318, 288
Messer, O. E. B., Mezzacappa, A., Bruenn, S. W., & Guidry, M. W. 1998, ApJ, 507, 353
Mezzacappa, A., & Bruenn, S. W. 1993a, ApJ, 405, 637
———. 1993b, ApJ, 405, 669
———. 1993c, ApJ, 410, 710
Mezzacappa, A., et al. 1998, ApJ, 495, 911
Mihalas, D. 1980, ApJ, 238, 1034
Mihalas, D., & Mihalas, B. 1984, Foundations of Radiation Hydrodynamics (New York: Oxford Univ. Press)
Morel, J. E., Wareing T. A., & Smith, K. 1996, J. Comput. Phys., 128, 445
Olson, G. L., Auer, L. H., & Buchler, J. R. 1986, J. Quant. Spectrosc. Radiat. Transfer, 35, 430
Qian, Y.-Z., & Woosley, S. E. 1996, ApJ, 471, 331
Raffelt, G., & Seckel, D. 1998, Phys. Rev. Lett., 69, 2605
Reddy, S., Prakash, M., & Lattimer, J. M. 1998, Phys. Rev. D, 58, 013009
Scharmer, G. B. 1981, ApJ, 249, 720
Schinder, P. J. 1990, ApJS, 74, 249
Schinder, P. J., & Bludman, S. A. 1989, ApJ, 346, 350
Schinder, P. J., & Shapiro, S. 1982a, ApJ, 259, 311
———. 1982b, ApJS, 50, 23
———. 1983, ApJ, 273, 330
Suzuki, H. 1993, in Frontiers of Neutrino Astrophysics, ed. Y. Suzuki & K. Nakamura (Tokyo: Universal Academy), 219
Suzuki, Y. 1998, Space Sci. Rev., 85, 91
Totsuka, Y., et al. 2000, Nucl. Phys. A (663-664), 1-4, 218–2300
Tubbs, D. L., & Schramm, D. N. 1975, ApJ, 201, 467
Vogel, P. 1984, Phys. Rev. D, 29, 1918
Weaver, T. A., & Woosley, S. E. 1995, ApJS, 101, 181
Woosley, S. E., Hartmann, D., Hoffman, R., & Haxton, W. C. 1990, ApJ, 356, 272
Woosley S. E., & Hoffman, R. D. 1992, ApJ, 395, 202
Yamada, S., Janka, H.-T., & Suzuki, H. 1999, A&A, 344, 533